ChemComm

FEATURE ARTICLE

View Article Online
View Journal | View Issue

Cite this: *Chem. Commun.*, 2022, **58**, 10136

Ultra-mild synthesis of nanometric metal chalcogenides using organyl chalcogenide precursors

Shashank Mishra *

Bis(trialkylsilyl) monochalcogenides and diorganyl dichalcogenides, $(R_3Si)_2E$ and R_2E_2 (E = S, Se or Te and R = alkyl, aryl or allyl group), have emerged in the past decade as excellent reagents for the synthesis of metal chalcogenide nanoparticles (NPs) and clusters owing to their ability to transfer the chalcogenide anion (E^{2-}) under ultra-mild conditions and versatility in reacting even with non-conventional metal reagents or being employed in a variety of synthetic methods. In comparison, the related non-silylated diorganyl monochalcogenides R_2E have received attention only recently for the solution phase synthesis of metal chalcogenide NPs. In spite of sharing many similarities, these three families of organyl chalcogenides are different in their coordination ability and decomposition behavior, and therefore in reactivities towards metal reagents. This feature article provides a concise overview on the use of these three families as synthons for the ultralow-temperature synthesis of metal chalcogenide nanomaterials, deliberating their different decomposition mechanisms and critically assessing their advantages for certain applications. More specifically, it discusses their usefulness in (i) affording molecular precursors with different kinetic and thermal stabilities, (ii) isolating reactive intermediates for comprehending the mechanism of molecule-to-nanoparticle transformation and, therefore, achieving fine control over the synthesis, (iii) stabilizing isolable metastable or difficult-to-achieve phases, and (iv) yielding complex ternary nanoparticles with controlled stoichiometry or composites with sensitive materials without modifying the characteristics of the latter. Besides providing a perspective on the low-temperature synthesis of nanomaterials, this overview is expected to assist further progress, particularly in the field of R_2E, leading to interesting materials including metastable ones for new applications.

Received 20th June 2022,
Accepted 4th August 2022

DOI: 10.1039/d2cc03458a

rsc.li/chemcomm

1. Introduction

Metal chalcogenide nanomaterials have been attracting world-wide attention as semiconducting materials with size-dependent and, hence, tunable electronic and optical properties (*e.g.*, band gap energy, carrier density, and dielectric response), which make them very attractive for several applications such as thermoelectricity, photovoltaics, photocatalysis, displays, biomedical imaging, *etc.*[1–16] The chemical and electronic properties of these functional materials are often governed by the synthetic methods employed. An ideal synthetic method must afford these materials in a reproducible manner and with a very high level of control over their size, shape, morphology and size dispersion.[1–5,15,16] Since the 'hot injection' method reported in 1993 by Murray *et al.* for the controlled synthesis of monodisperse nanoparticles (NPs) of CdE (E = S, Se, Te),[17] several solution-phase methods involving either single source precursors or separate metal and chalcogenide reagents have been developed for the synthesis of colloidal metal chalcogenide NPs. These employ different chalcogenide ligands/reagents such as tertiary phosphine chalcogenides, chalcogenoureas, chalcogenolates, chalcogenocarbamates, xanthates, dichalcogenoimidodiphosphinates, or sulfur and selenium dissolved in octadecene or amines.[18–20] Although these precursors have many advantages such as easy availability and high solubility in organic solvents, a majority of them require high temperature, which favors the formation of thermodynamically stable species only. Lowering the synthesis temperature is a highly desirable step to use these materials in technologically advanced areas such as energy conversion and storage, catalysis, environment, biomedicine and electronics.

Unlike metal oxides,[21–24] the low-temperature synthesis of functional metal chalcogenide nanomaterials is yet to realize its potential, and an important area in this direction is the exploration and identification of the reagents and precursors

Université Claude Bernard Lyon 1, CNRS, UMR 5256, Institut de Recherches sur la Catalyse et l'Environnement de Lyon (IRCELYON), 2 Avenue Albert Einstein, 69626 Villeurbanne, France. E-mail: shashank.mishra@ircelyon.univ-lyon1.fr; Fax: +33-472445399; Tel: +33-472445322

that are reactive at low temperature.[25,26] Other reasons behind exploring alternative chalcogenide reagents include cost, ease of handling, toxicity, purity, and the ability to tune the nucleation and growth kinetics. In this regard, bis(trialkylsilyl) monochalcogenides $(R_3Si)_2E$ and diorganyl dichalcogenides R_2E_2 (where E = S, Se or Te, and R = an alkyl, aryl or allyl group) have emerged as excellent entry points for the synthesis of metal chalcogenide nanomaterials and clusters, owing to (i) their ability to transfer the chalcogenide anion (E^{2-}) under ultra-mild conditions, (ii) easy tunability of their reactivity and properties by varying the organyl group R, (iii) facile removal of the byproducts, (iv) commercial availability, and (v) high solubility in common organic solvents.[25–31] These versatile reagents not only are applicable in a variety of synthetic methods (co-precipitation, thermal or microwave decomposition, ionic liquid media, microemulsions, chemical vapor deposition, *etc.*), but can also react in a facile manner even with non-conventional metal reagents (metal oxides, metal chalcogenides, metallic nanoparticles, *etc.*) to yield metal chalcogenide NPs and nanoclusters. Since these reagents generate metal chalcogenide NPs under mild conditions, they can generate metastable and previously unknown crystalline phases for certain materials and can even be exploited for the synthesis of composites with sensitive materials without modifying their structural and morphological characteristics.

The related non-silylated diorganyl monochalcogenides R_2E, which exhibit many similarities to the above two families of organyl chalcogenides, have received much less attention for solution-phase low temperature synthesis of metal chalcogenide nanomaterials. While as a class R_2E does share many of the advantages listed above for $(R_3Si)_2E$ and R_2E_2, it also differs in many features. As compared to $(R_3Si)_2E$, which often forms a thermally unstable R_3SiE-M bond due to the excellent leaving property of the silylated group, the neutral R_2E forms a stronger and stable bond with the metal centre, making them usually less efficient in transferring the chalcogen to metal centers and leading to the formation of stable metal organyl chalcogenide adducts.[32,33] This restricts their use mainly to the elaboration of thin films by the chemical vapor deposition technique, either as a reagent (in dual source CVD)[34–37] or as single source precursors (after complexation with metals),[38–41] requiring usually high temperature. On the other hand, R_2E is usually more reactive than R_2E_2, which has an additional E–E bond to be ruptured during the decomposition. These features make the reactivity of R_2E somewhat unique, which, simply by varying R and E, can be modulated between highly reactive $(R_3Si)_2E$ and somewhat less reactive R_2E_2. This may have implications in the potential use of R_2E in many applications including in the synthesis of new metastable phases with unique properties and applications, as shown in the case of R_2E_2.[42] Despite these unique features and high potential, the use of R_2E in the low-temperature solution-phase synthesis of metal chalcogenide nanomaterials has received much less attention. Exploiting the facile decomposition mechanism in some of the non-silylated diorganyl monochalcogenides R_2E, a recent study from our laboratory has shown (i) the synthesis of metal precursors that decompose at very low temperature to generate metal chalcogenide nanomaterials,[43] and (ii) the direct synthesis of metal chalcogenide NPs at room temperature.[44–47] In the latter case, the isolation and characterization of the reactive molecular intermediates has helped in understanding the molecule-to-nanoparticle transformation better towards the development of synthetic methods with greater control.

In spite of the great utility of these organyl chalcogenides in the solution phase synthesis of metal chalcogenide nanomaterials under ultra-mild conditions, no inclusive effort has been made so far to review the subject matter. While the use of bis(trialkylsilyl) monochalcogenides $(R_3Si)_2E$ in generating metal chalcogenide molecular clusters has been reviewed,[28–31] their use in the synthesis of nanomaterials only finds a somewhat limited mention in a recent book chapter.[48] The use of R_2E_2 as synthons for semiconducting nanoparticles was reviewed in 2015,[26] but there have been some important developments in the field since then, particularly in the synthesis of metastable phases.[49–51] This review highlights and contextualizes the emerging work on the use of organyl chalcogenides as interesting chalcogenide reagents for the mild synthesis of metal chalcogenide nanomaterials in the solution phase. After a brief introduction, the section on non-silylated organyl monochalcogenides R_2E focuses on their divergent reactivity to afford either nanoparticles or molecular complexes with different kinetic and thermal stability and underlines the importance of identifying the reactive intermediates in comprehending what happens at the interface when molecules are transformed into nanomaterials and, therefore, achieving fine control over the synthesis. The advantages of mild and controlled preparation of these NPs are discussed in terms of ligand-free synthesis of metal chalcogenide–TiO_2 nanocomposites for photocatalytic applications. It is followed by a subsection on the closely

Shashank Mishra

Shashank Mishra is Associate Professor of Chemistry at the Université Claude Bernard Lyon 1, France. His research interests are in the intersection of molecular and materials chemistry and mainly concerned with the design of molecular precursors and understanding their transformations to metal chalcogenide, metal oxide and metal fluoride nanomaterials via solution or vapor phase routes for applications in optics, energy, catalysis and related fields. He has also made contributions in the field of halometallate-based perovskite-inspired materials for photovoltaics. About 85 research articles, 6 reviews, 2 book chapters, and over 35 invited talks in international conferences summarize his research activities in the above field. Being a recipient of a couple of young scientist awards in the past, he was recently named an Emerging Investigator 2022 by the ACS journal Crystal Growth & Design.

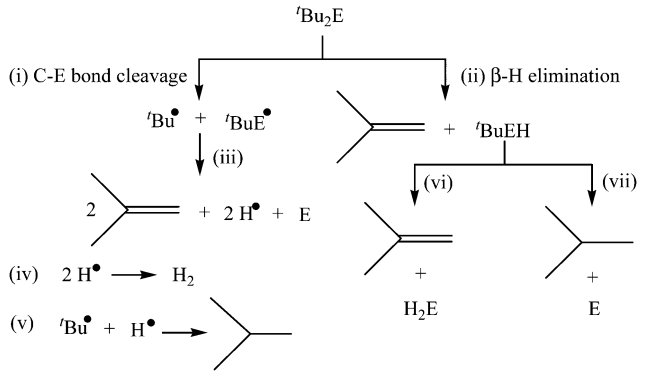

Scheme 1 The possible decomposition pathways of ^{t}Bu$_2$E (E = S, Se).

related precursors $(R_2M)_2E$ and $(R'_2M)ER$ (M = Sb or Bi), which can be considered as derived from R_2E by replacing both or one R group(s) with the R'_2M moiety (M = Sb, Bi), for binary M_2E_3 or ternary $(Sb_xBi_{1-x})_2E_3$ nanomaterials.[52] The next section on bis(trialkylsilyl) monochalcogenides $(R_3Si)_2E$ describes in detail the use of different methods and the influence of diverse reaction conditions on the synthesis of different types of metal chalcogenide nanomaterials including complex ternary nanocrystals with controlled stoichiometry. The final section on R_2E_2 compares its reactivity with R_2E and summarizes recent important advances in its use for the isolation of new metastable phases. In the end, it identifies and signifies the areas for future research in the Conclusions and looking ahead section. I hope that this article will not only provide a reference text for a wider community working on metal chalcogenide nanomaterials, including a general perspective on the low-temperature synthesis of nanomaterials, but also initiate a future progression, particularly on non-silylated R_2E, to enhance further the overall understanding of molecule-to-nanoparticle transformation and contribute to the synthesis of interesting metal chalcogenide materials for new high-tech applications.

2. Non-silylated diorganyl monochalcogenides R_2E: distinctive reactivity towards metal reagents

As mentioned in the Introduction section, the utilization of nonsilylated diorganyl monochalcogenides R_2E has been mainly restricted to the elaboration of thin films in the chemical vapor deposition technique which requires high temperature.[34–41] Although generally less reactive in comparison to silylated organyl chalcogenides $(R_3Si)_2E$, the reactivity patterns and properties of non-silylated analogues R_2E can be modulated in a subtle manner by varying systematically the organyl group R. For instance, the reactions of $FeCl_2$ with diallyl sulfide $(allyl)_2S$, dibenzyl sulfide Bz_2S and di-*tert*-butyl sulfide ^{t}Bu$_2$S in oleylamine at 220 °C yielded different morphologies of pyrrhotite Fe_7S_8 NPs, whereas di-phenyl sulfide Ph_2S under similar conditions did not react with $FeCl_2$.[27] Some of these organyl chalcogenides R_2E, particularly those containing di-tertiary-butyl groups ^{t}Bu$_2$E (E = S, Se, Te), have been shown to undergo facile decomposition at low temperature, although their exact decomposition mechanism has been a subject of debate.[53,54] The possible initial steps in the decomposition include (i) C–E bond cleavage to give ^{t}Bu$^\bullet$ and ^{t}BuE$^\bullet$ radicals and (ii) β-H elimination to give isobutene and tertiary-butyl chalcogenol (Scheme 1). While it was proposed using deuterium labelled experiments that ^{t}Bu$_2$Se undergoes decomposition *via* initial Se–C bond cleavage,[53] recently it was shown using *ab initio* calculations that the non-radical β-H elimination pathway could almost fully account for the decomposition of ^{t}Bu$_2$S, even though radical reactions do have an effect on the product distribution.[54] This difference in the decomposition mechanism of ^{t}Bu$_2$Se and ^{t}Bu$_2$S may be traced to a slightly different strengthening of the C–S and C–Se bonds, the former being thermodynamically more stable. This facile decomposition in ^{t}Bu$_2$E (E = S, Se, Te) and related reagents can be exploited as a strategy to either prepare single source precursors with low thermal decomposition temperature or get metal chalcogenide NPs directly at room temperature, as described below.

2.1. Stable molecular complexes with low thermal decomposition temperature

The high coordinating ability of organyl chalcogenides to afford molecular complexes is well-known.[32,33] However, the application of these complexes as single source precursors is relatively new and mostly confined to vapor phase synthesis which requires high temperature.[38–41] Employing well-characterized single-source precursors (SSPs) with well-defined composition not only overcomes the problem of controlling the stoichiometry of the constituent elements in the metal chalcogenides and paves the way for their low temperature and sustainable syntheses (therefore reducing the fabrication cost), but also provides numerous opportunities for the design and improvement in the properties of these materials.[55–57] As metal chalcogenide nanostructures and thin films are the core components of high-performance devices, the low temperature solution phase fabrication of these materials offers a unique opportunity for their incorporation in relevant areas like electronics, energy conversion and storage, environmental science, catalysis and biomedicine. As mentioned previously, the kinetic and thermal stability of these molecular complexes $[MX_y(R_2E)_z]_n$ can vary depending on the nature of the metal (M), ancillary ligand (X) or substituent R and chalcogen atom E in the organyl chalcogenides. Using R_2E with alkyl groups that have a facile decomposition mechanism *via* β-hydrogen elimination, several molecular complexes with low thermal stability have been synthesized. For instance, Reid *et al.* have synthesized many metal halide complexes with the di-*n*-butyl chalcogenide ligand $[MCl_4(^nBu_2E)_2]$ (M = Ti, Sn, Mo; E = S or Se), the thermogravimetric analyses (TGA) of which showed their low thermal decomposition (typically below 250 °C).[58–60] The C–Se bond is slightly weaker than the C–S bond and, therefore, the ^{n}Bu$_2$Se analogues are expectedly decomposed at slightly lower temperature than those with the ^{n}Bu$_2$S ligand. These precursors were employed in MOCVD to deposit metal chalcogenide thin

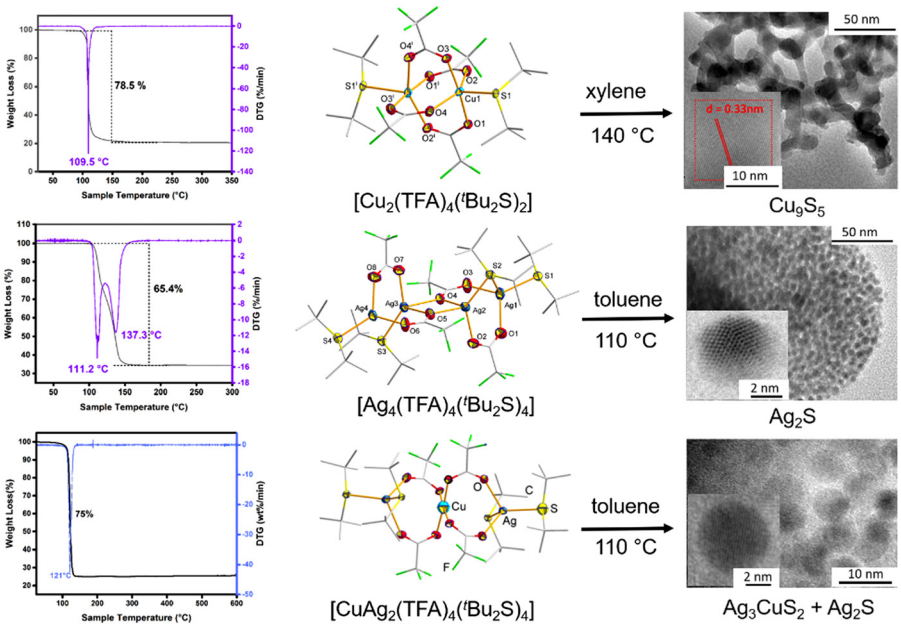

Fig. 1 Homo- and heterometallic coinage metal complexes with $^{t}Bu_2S$ as a precursor with ultra-low decomposition temperature. Adapted with permission from ref. 43 and 46. Copyright (2021) Wiley-VCH; (2020) American Chemical Society.

films. On substituting the ^{n}Bu group with ^{t}Bu, the decomposition can further be accelerated, thus lowering the decomposition temperature further. Fig. 1 shows the TGA curves of some homo- and heterometallic complexes of the coinage metals with the $^{t}Bu_2S$ ligand, which exhibit one- or two-step decomposition at low temperature (typically between 110 and 140 °C) with residues that correspond to metal sulfides as the end products. While homometallic copper and silver precursors $[Cu_2(TFA)_4(^{t}Bu_2S)_2]$ and $[Ag_4(TFA)_4(^{t}Bu_2S)_4]$ (where TFA = trifluoroacetate) are decomposed to give Cu_9S_5 and Ag_2S, respectively,[43] the heterometallic $[Ag_2Cu(TFA)_4(^{t}Bu_2S)_4]$ decomposes in a single step at 120 °C to give a mixture of Ag_3CuS_2 and Ag_2S.[46] In contrast, organyl chalcogenides which do not have an alternative decomposition mechanism (*e.g.*, Me_2E) afford metal complexes that are kinetically and thermally stable.[44,46,61] For example, the homometallic $[Ag_5(TFA)_5(Me_2Se)_4]$ and heterometallic $[Ag_2Cu(TFA)_4(Me_2Se)_4]$ complexes require much high temperature (~300 °C) to decompose to yield Ag_2Se and a mixture of AgCuSe + Ag_2Se, respectively.[44,46]

2.2. Isolation of reactive molecular intermediates during the course of formation of metal chalcogenide nanoparticles

In the bottom-up approach of materials synthesis, identification of intermediate species operating at the intersection of molecular and nanometric levels is a key aspect in understanding the mechanism of molecule-to-nanoparticle formation and therefore achieving fine control over the synthetic conditions to prepare materials with controlled composition and properties. However, it is challenging to isolate and characterize these intermediates unambiguously because they are usually highly reactive in nature. Recently, we have found success in using R_2E of suitable reactivity to isolate and characterize reactive molecular intermediates during the course of formation of binary and ternary coinage metal selenide NPs.[44–46] Specifically, by reacting $^{t}Bu_2Se$ with $Cu(TFA)_2$ or/and Ag(TFA) (where TFA = trifluoroacetate) in a variety of solvents (diethyl ether, tetrahydrofuran or toluene), we reported direct synthesis of binary and ternary coinage metal selenide NPs $Cu_{2-x}Se$, Ag_2Se and AgCuSe NPs at room temperature. We succeeded in isolating and characterizing by the single crystal X-ray technique the highly reactive intermediates $[Cu_2(TFA)_2(^{t}Bu_2Se)_3]$, $[Ag(TFA)(^{t}Bu_2Se)_2]$ and $[Ag_2Cu(TFA)_4(^{t}Bu_2Se)_4]$ during the course of these reactions, which provided unambiguous proof that $Cu_{2-x}Se$, Ag_2Se and AgCuSe NPs are formed *via* the above intermediates, respectively (Fig. 2). These isolated intermediates are unstable as they turn black within a few days even at low temperature and in an inert atmosphere, apparently due to their transformation into metal selenides. The thermal and kinetic instability of these intermediates was further confirmed by thermogravimetric (TGA) and density functional theory (DFT) calculations, respectively. For example, the TGA of the heterometallic intermediate $[Ag_2Cu(TFA)_4(^{t}Bu_2Se)_4]$ shows its decomposition below 100 °C with a residual mass that is consistent with the formation of 1 eq. AgCuSe and 0.5 eq. Ag_2Se as the end product, whereas a HOMO–LUMO gap of 0.25 eV was calculated from the DFT calculations.[46] The fact that this intermediate is transformed to a mixture of AgCuSe and Ag_2Se when left in air for a few hours underlines its high reactivity. In comparison, the $^{t}Bu_2S$ analogue $[Ag_2Cu(TFA)_4(^{t}Bu_2S)_4]$ shows a better kinetic stability and can be kept intact at room temperature for several weeks. The higher stability of this analogue is attributed to a stronger C–S bond (as compared to the C–Se bond). Besides being a facile source of Se^{2-}, the coordinated $^{t}Bu_2Se$ ligand also plays the role of a reducing

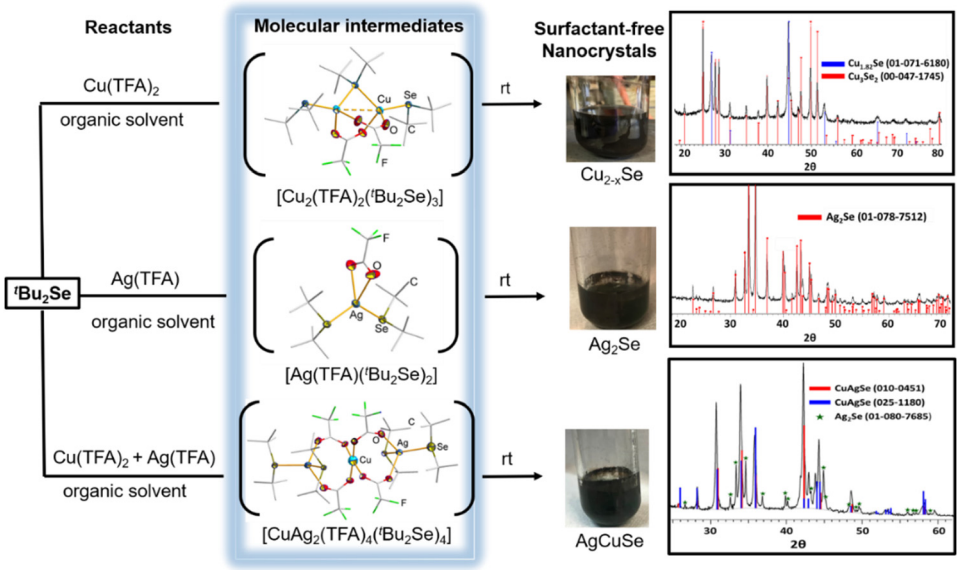

Fig. 2 Isolation and structural characterization of reactive intermediates during the syntheses of $Cu_{2-x}Se$, Ag_2Se and AgCuSe NPs from the reactions of $^tBu_2Se$ with coinage metal trifluoroacetates. Adapted with permission from ref. 44–46. Copyright (2016) Wiley-VCH; (2018) The Royal Society of Chemistry; and (2020) American Chemical Society.

reagent to get the desirable +1 oxidation state of copper during the transformation of $[Cu_2(TFA)_2(^tBu_2Se)_3]$ and $[Ag_2Cu(TFA)_4(^tBu_2Se)_4]$ to $Cu_{2-x}Se$ and CuAgSe + $Cu_{2-x}Se$ NPs, respectively. In comparison to intermediates involving Cu(II) species, the transformation of $[Ag(TFA)(^tBu_2Se)_2]$ to Ag_2Se NPs required no metal reduction step and, therefore, the reaction was much faster (5–30 min), more reproducible and afforded a better yield (>95%).[44] The binary $Cu_{2-x}Se$ and Ag_2Se NPs on further reaction with $^tBu_2Se$ at RT gave compositionally tailored ternary metal chalcogenide CuAgSe NPs.[47] The above ultra-mild synthesis of binary and ternary NPs using the $^tBu_2Se$ ligand was further exploited to generate composites with TiO_2 (P25) for photocatalysis without compromising the structural and morphological characteristics of TiO_2 and without having any organics around NPs. As a result, the obtained metal–chalcogenide–TiO_2 nanocomposites acted as better photocatalysts than the commercially available benchmark TiO_2 (P25) for formic acid degradation under UV irradiation.[44,45,47] Some selected examples of metal chalcogenide nanoparticles synthesized under mild conditions using non-silylated organyl chalcogenides are summarized in Table 1.

2.3. Related $(R'_2M)_2E$ and $(R'_2M)_2ER$ (M = Sb, Bi) as precursors for Group 15 metal chalcogenides

The related $(R'_2M)_2E$ and $(R'_2M)ER$, which can be considered as derived from R_2E by replacing both or one R group(s) with the R'_2M moiety (M = Sb, Bi), have recently been employed as single source precursors under a variety of mild conditions to get binary M_2E_3 and ternary $Sb_2(S_{1-x}Se_x)_3$ or $Bi_xSb_{1-x}E_3$ materials.[52] Although it is known in the literature for quite some time that the related complexes of the type $(RM)_2E$ (where M = Zn, Cd, Hg; E = S, Se, Te; R = Me, Ph) decompose readily to

Table 1 Some selected examples of metal chalcogenide nanomaterials synthesized under mild conditions using non-silylated R_2E

Reagents/precursors	Materials	Synthesis (temp., solvent, capping ligand, *etc.*)	Ref.	Comments
$[Cu_2(TFA)_4(^tBu_2S)_2]$	ODT-Protected Cu_9S_5 NPs	145 °C, xylene, ODT	43	Precursor with one-step decomposition (single DTG peak at 110 °C)
$Cu(TFA)_2$ + $^tBu_2Se$	$Cu_{2-x}Se$ NPs	110 °C, toluene	45	Reaction proceeds *via* a reactive intermediate $[Cu_2(TFA)_2(^tBu_2Se)_3]$
$[Ag_4(TFA)_4(^tBu_2S)_4]$	ODT-protected Ag_2S NPs	145 °C, xylene, ODT	43	Precursor decomposes at as low temperature as 60 °C
Ag(TFA) + $^tBu_2Se$	Ag_2S NPs	RT, Et_2O	44	A reactive intermediate $[Ag(TFA)(^tBu_2Se)_2]$ was isolated during the reaction and characterized structurally
$FeCl_2$ + R_2S (R = ^{t}Bu, allyl, Bz, Ph)	Pyrrhotite Fe_7S_8 NPs	220 °C, OLA	27	While $^tBu_2S$, $(allyl)_2S$, and $(benzyl)_2S$ yielded the pyrrhotite phase (Fe_7S_8) with different morphologies, Ph_2S did not react under identical conditions
$Cu_{2-x}Se$ NPs + Ag(TFA) + $^tBu_2Se$	Uncapped CuAgSe NPs	RT, THF	47	Ultra-mild synthesis allows to combine CuAgSe with TiO_2 without modifying the characteristics of TiO_2
$[CuAg_2(TFA)_4(^tBu_2S)_4]$	Ag_3CuS_2 NPs	110 °C, toluene	46	Precursor with one-step decomposition (single DTG peak at 120 °C)
Ag(TFA) + $Cu(TFA)_2$ + $^tBu_2Se$	AgCuSe NPs	RT, no solvent or capping ligand	46	A highly reactive intermediate $[CuAg_2(TFA)_4(^tBu_2Se)_4]$ was isolated during the reaction and characterized

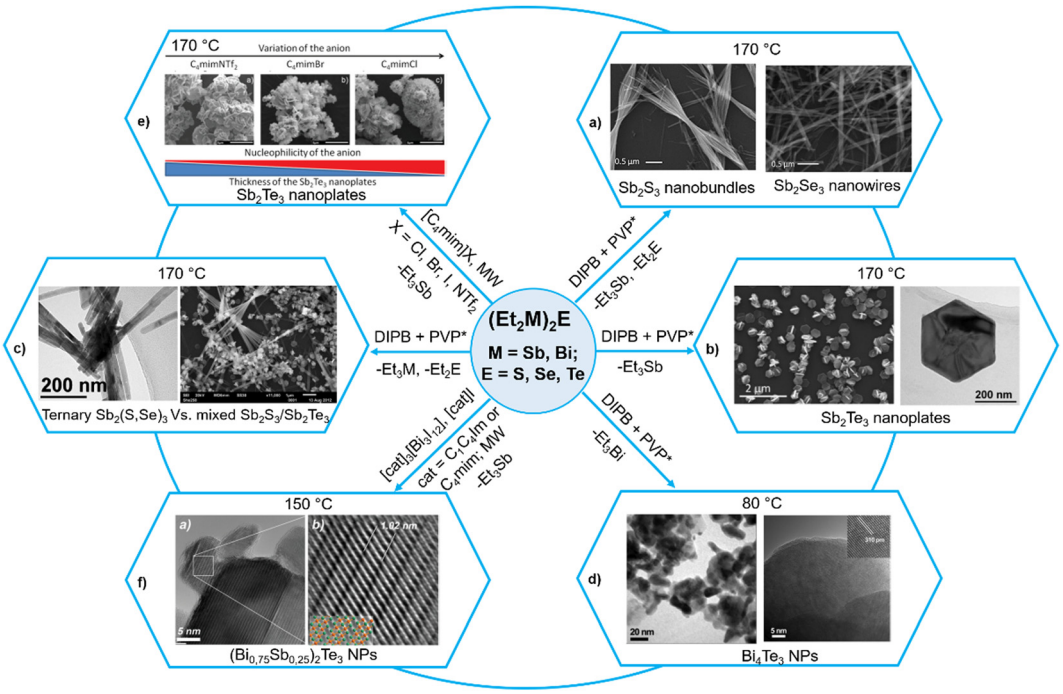

Fig. 3 Diversity of $(Et_2M)_2E$ (M = Sb, Bi; E = S, Se, Te) precursors to get binary M_2E_3 and ternary $Sb_2(S_{1-x}Se_x)_3$ or $(Bi_xSb_{1-x})_2Te_3$ nanoparticles. Adapted with permission from ref. 63–65, 67 and 68. Copyright (2015, 2021) Wiley-VCH; (2015, 2017) The Royal Society of Chemistry; and (2012) American Chemical Society.

give ME and R_2M,[62] it is only recently that Schulz *et al.* have carried out a systematic study on $(R'_2M)_2E$ for group 15 binary and ternary metal chalcogenide nanomaterials.[63–68] For instance, they used $(Et_2Sb)_2E$ (E = S, Se, Te) as a SSP for highly crystalline Sb_2E_3 NPs in different organic solvents in the presence of poly(1-vinylpyrrolidone)graft-1-hexadecene (PVP*) as a capping agent at temperatures below 170 °C.[63,64] While $(Et_2Sb)_2Te$ decomposes upon heating at 140 °C in a straightforward manner to produce highly stoichiometric Sb_2Te_3 and Et_3Sb, the decomposition pathways of $(Et_2Sb)_2E$ (E = S, Se) are more complex and produce Sb_2E_3, $SbEt_3$ and Et_2E. This leads to formation of slightly Sb-rich Sb_2S_3 and Sb_2Se_3 materials. Depending upon the nature of chalcogenide atoms, the morphology of the materials also differed significantly. Thus, Sb_2S_3 and Sb_2Se_3 were obtained as nanobundles and nanowires, respectively (Fig. 3a), whereas Sb_2Te_3 formed hexagonal, almost monodisperse, crystalline nanoplates of roughly 400 nm diameter and 35 nm thickness (Fig. 3b). The above difference in the decomposition pathways of $(Et_2Sb)_2E$ is further manifested during their co-decomposition to get possibly ternary phases. While excellent compatibility in the decomposition behaviour and morphology of $(Et_2Sb)_2S$ and $(Et_2Sb)_2Se$ led to the formation of the ternary $Sb_2(S, Se)_3$ phase without any impurities on their simultaneous decomposition at 170 °C, co-decomposition of $(Et_2Sb)_2S$ and $(Et_2Sb)_2Te$ under similar conditions yielded biphasic, heterocomposite materials containing crystalline Sb_2S_3 nanobundles and Sb_2Te_3 nanoplates (Fig. 3c).[64] In contrast to the behavior of $(Et_2Sb)_2E$, the thermolysis of the analogous bismuth precursor $(Et_2Bi)_2Te$ in 1,3-diisopropylbenzene (DIPB) led to the formation of Bi_4Te_3 at 80 °C (Fig. 3d) and mixtures of Bi_4Te_3 and elemental Bi at higher temperatures, most probably due to the comparably low Te–Bi binding energy and complex decomposition mechanism involving radicals.[65]

The quality of the above materials could further be improved by microwave-assisted decomposition of the above precursors in ionic liquids.[66,67] Thus, microwave-assisted decomposition of $(Et_2Sb)_2Te$ in $[C_4mim]Br$ (C_4mim = 1-butyl-3-methylimidazolium) produced phase pure Sb_2Te_3 NPs with improved thermoelectric properties.[65] The authors then studied in detail the influence of the nature of counter anions (Cl^-, Br^-, I^- and NTf_2^-, where NTf_2^- = bis(trifluoromethanesulfonyl)amide) as well as the chain length of the alkyl group of the cation (1-alkyl-3-methylimidazolium or 1,3-dialkylimidazolium) in a set of ionic liquids.[67] While increasing the chain length resulted in better solubility of the precursor $(Et_2Sb)_2Te$, which enhanced the formation of less aggregated nanoparticles, the strongly basic anion such as Cl^- with higher coordinating capability resulted in the formation of thin Sb_2Te_3 nanoplates (Fig. 3e). As a consequence, the thermoelectric properties of the resulting Sb_2Te_3 nanoplates strongly differed. When the above precursor was decomposed in a mixture of ionic liquids containing varying amounts of Bi-containing ILs $[C_4mim]_3[Bi_3I_{12}]$ and $[C_4mim]I$, highly stoichiometric and phase-pure ternary solid solutions of the type $(Bi_xSb_{1-x})_2Te_3$ could be synthesized at 150 °C (Fig. 3f).[68] The synthetic details of these examples are summarized in Table 2.

Another related class $(R_2M)ER'$ (M = Sb, Bi) has also been employed as SSPs for M_2E_3 materials. Kim *et al.* investigated the thermal decomposition of Ph_2SbTeR (R = Et, Ph) in

Table 2 Binary M_2E_3 and ternary $Sb_2(S_{1-x}Se_x)_3/Bi_xSb_{1-x}E_3$ nanomaterials using $(Et_2M)_2E$ or $(R'_2M)E(R)$ as precursors

Precursor	Materials	Synthesis (temp., solvent, capping ligand, *etc.*)	Ref.	Comments
$(Et_2Sb)_2S$	Sb_2S_3 nanobundles	170 °C, DIPB, PVP*	63	Slightly Sb-rich Sb_2S_3 due to formation of the volatile by-product Et_2S
$(Et_2Sb)_2Se$	Sb_2Se_3 nanowires	170 °C, DIPB, PVP*	63	Slightly Sb-rich Sb_2Se_3 due to formation of the volatile byproduct Et_2Se
$(Et_2Sb)_2S$ + $(Et_2Sb)_2Se$	$Sb_2(S_{1-x}Se_x)_3$ nanowires	170 °C, DIPB, PVP*	63	Impurity-free ternary phase due to excellent compatibility in the decomposition patterns of $(Et_2Sb)_2S$ and $(Et_2Sb)_2Se$
$(Et_2Sb)_2Te$	Sb_2Te_3 hexagonal plates	170 °C, DIPB, PVP*	64	Phase-pure product due to stoichiometric decomposition in Sb_2Te_3 and Et_3Sb
$(Et_2Bi)_2Te$	Pure Bi_4Te_3 (80 °C), Bi_4Te_3 + metallic Bi (80–170 °C)	80-170 °C, DIPB, PVP*	65	Metallic Bi impurity at temp. higher than 80 °C due to a weak Te–Bi bond
$(Et_2Sb)_2Te$	Sb_2Te_3 NPs	170 °C (MW-decompos.), $[C_4mim]X$ (X = Cl^-, Br^-, I^-, NTf_2^-)	66,67	Less agglomerated NPs by increasing the cation chain length of ILs (due to the enhanced solubility of the precursor) and thinner Sb_2Te_3 nanoplates by using strongly basic anions, *e.g.*, Cl^-
$(Et_2Sb)_2Te$ + $[C_4mim]_3[Bi_3I_{12}]$	$(Bi_xSb_{1-x})_2Te_3$ NPs	150 °C (MW decompos.), $[C_4mim]I$	68	Highly stoichiometric, phase-pure ternary NPs by using a Bi-containing IL
$(Et_2Bi)Te(Et)$	Bi_2Te NPs	100 °C, DIPB, OA	65	Bi-Rich product due to a weak Te–Bi bond
$(Ph_2Sb)Te(Et)$	Sb_2Te_3 nanoplates	300 °C, oleylamine	69	High quality nanoplates at 300 °C per 2 h. A lower temp. and shorter time (250 °C per 1 h) lead to Sb_2Te_3 + Sb_2Te mixed phases
$(Ph_2Sb)Te(Ph)$	Sb_2Te_3 nanoplates	250 °C, oleylamine	69	Perfect hexagonal nanoplates under mild conditions (250 °C per 1 h). A higher temp. and time (300 °C per 2 h) distort the shape
$(Et_2Bi)Te(Et)$	Bi_2Te NPs	100 °C, DIPB or OA	65	Te-Poor Bi_2Te particles due to formation of the volatile byproduct Et_2Te

Abbreviations: C_4mim = 1-butyl-3-methylimidazolium; C_4C_1Im = 1-butyl-3-methylimidazolium; DIPB = 1,3-diisopropylbenzene; NTf_2^- = bis(trifluoromethanesulfonyl)amide; ILs: ionic liquids; PVP* = poly(1-vinylpyrrolidone)graft-1-hexadecene.

oleylamine.[69] In the case of $Ph_2SbTeEt$, high-quality Sb_2Te_3 nanoplates were obtained after heating at 300 °C for 2 h, whereas lower reaction temperatures (250 °C) and shorter reaction times (1 h) resulted in the formation of a mixture of Sb_2Te as the major component and Sb_2Te_3 powders, indicating a rather complex decomposition mechanism. On the contrary, pure Sb_2Te_3 nanoplates of hexagonal shape were obtained using $Ph_2SbTePh$ at 250 °C for 1 h, whereas an increasing reaction time (2 h) and temperature (300 °C) yielded shape-distorted Sb_2Te_3 nanoplates. In contrast, the thermolysis of $Et_2BiTeEt$ in DIPB or OA gave pseudo-cubic Bi_2Te particles, possibly due to the formation of the volatile byproduct Et_2Te, leading to Te-poor Bi_2Te particles.[65] Interestingly, the use of a similar precursor in MOCVD led to the formation of phase-pure Bi_2Te_3 films on Si(100) at a very low substrate temperature of 230 °C, indicating that the decomposition mechanism for this precursor is very different in the solution and gas phases.[70] EDX and XRD studies revealed the formation of highly stoichiometric and phase pure Bi_2Te_3 films at 215 and 230 °C, while higher substrate temperatures (245 °C) yielded Bi-rich materials with Bi_4Te_3 as the additional phase.

3. Bis(trialkylsilyl) monochalcogenides $(R_3Si)_2E$ as facile chalcogenide-transfer reagents

The chalcogen-transfer ability of the silylated diorganyl monochalcogenides $(R_3Si)_2E$ is well-known, which has allowed an easy access to metal chalcogenide nanoparticles or clusters, depending on the reaction conditions. These silylated chalcogenides $(R_3Si)_2E$ react readily with a metal reagent MX_n (X = alkyl, halide, amide, carboxylate, oxide), where facile and homogeneous delivery of the chalcogenide (E^{2-}) to the metal center is promoted by the affinity of silicon(IV) for oxygen and halides as well as the volatility of the formed byproduct R_3SiX (Scheme 2).[71–76] When the reaction is performed in the presence of an ancillary ligand L (*e.g.*, PR_3), it often leads to the formation of high nuclear nanoclusters $[M_xE_y(L)_z]$.[28–31] The reaction is supposed to proceed through the formation of chalcogenolate intermediates, although the high thermal instability of the M–$ESiR_3$ bonds makes it difficult to isolate these intermediates before they afford E^{2-}. To some extent, the stability of these chalcogenolate intermediates can be

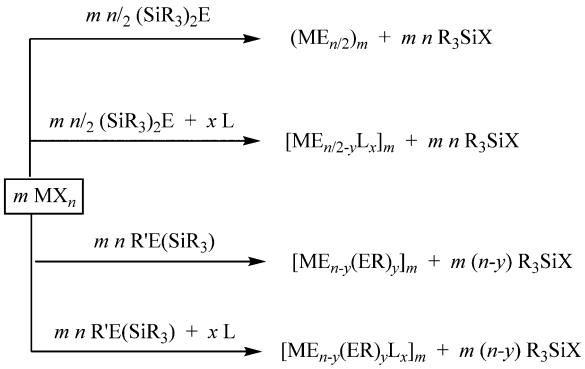

M = a transtion / main group metal; X = alkyl, halide, amide, carboxylate; E = S, Se, Te; L = tri alkyl/phenyl phosphine and related ligand; R, R' = an alkyl group; *m, n, x* ≥1; *y* ≥ 0

Scheme 2 Bis(trialkylsilyl) monochalcogenides as facile chalcogenide-transfer reagents.

increased by using a strongly bonded ancillary ligand such as N-heterocyclic carbine (NHC) or cyclic diamine, as indicated by the isolation and structural characterization of [(IPr)M($ESiMe_3$)], [(tmeda)Zn($ESiMe_3$)$_2$] (M = Cu, Ag; E = S, Se, Te; IPr = 1,3-bis(2,6-diisopropylphenyl)imidazolin-2-ylidene; tmeda = tetramethylethylenediamine), [(NHC)Ag–$ESiMe_3$] (E = S, Se) and [(NHC)Ag–S–Hg–S–Ag(NHC)] at low temperature.[77–79] Besides stabilizing the molecular intermediates, these ancillary ligands can also stabilize the monodisperse NPs formed at the end of the reaction, as exemplified by the synthesis of phase-pure and highly monodisperse coinage metal chalcogenide QDs (Ag_2E, $Cu_{2-x}E$; E = S, Se) from the room temperature reaction of $(Me_3Si)_2E$ with metal halide synthons containing N-heterocyclic carbene (NHC) ligands.[80] Alternatively, reagents with mixed silylated and non-silylated alkyl groups (R_3Si)ER′ can be exploited to introduce surface chalcogenolate groups (Scheme 2). These ligand-protected clusters can be considered as borderline species between molecules and nanoparticles, which may serve as precursors for well-defined metal chalcogenide NPs.[29]

The high reactivity of these reagents ensures not only a high yield of the products, but also a fast growth and, therefore, well-defined shape of the NPs. While the high reactivity ensures that these silylated reagents react quantitatively with the metal reagents, the good leaving property of the trialkylsilyl group makes sure that it does not act as a surface ligand (unlike other reagents such as trioctylphosphine (TOP) that can form a complex with the metal center and, therefore, limit the yield of metal chalcogenides). These properties make the bis silyl-chalcogenides $(R_3Si)_2E$ the reagents of choice for the synthesis of metal chalcogenide NPs, despite the perceived difficulty in their handling due to high volatility and air/moisture sensitivity.[31] The following subsections describe the versatility of these reagents in the synthesis of metal chalcogenide NPs under mild conditions.

3.1. Metal–organic decomposition at low-to-moderate temperatures

3.1.1. Influence of the choice of reagents and their ratio. The main principles developed so far in the synthesis of NPs with various morphologies and shapes can be understood by taking the example of lead chalcogenides,[81–89] which as NIR-active materials show great potential in many applications such as photovoltaics, optoelectronics, sensors and bio-electronics.[90] A typical synthetic procedure involves the injection of $(Me_3Si)_2E$ into the solution of lead reagents PbX_2 (where X = halide or oleate) at moderate temperatures of 60–140 °C, which yields PbE NPs (E = S, Se, Te) with a quantum efficiency of 20–30% and a narrow size distribution (10 ± 15%) (Fig. 4a). The mechanism of the formation of PbS from the reaction of lead(II) oleate and $(Me_3Si)_2S$ has been studied in detail.[91] According to the proposed mechanism, the reaction is proceeded by the formation of an intermediate complex [(OA)Pb(S-$SiMe_3$)$_2$] with Pb–S bonds that, upon the injection of a protic solvent, forms further Pb–S containing intermediates. However, due to their highly reactive nature, these intermediate complexes could not be isolated and studied unambiguously.

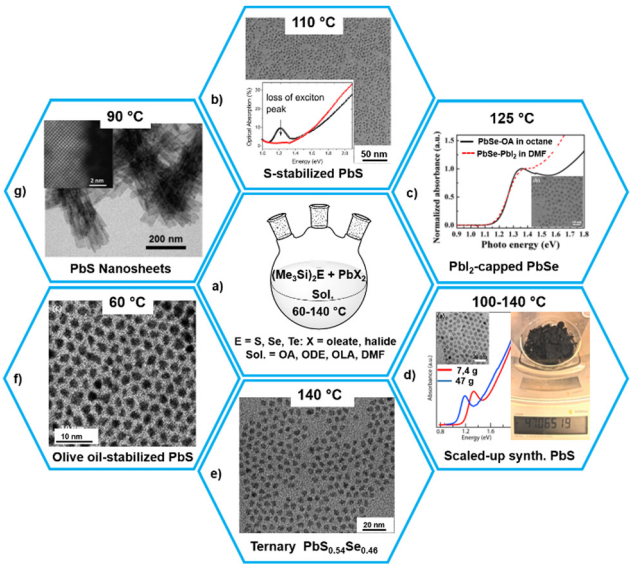

Fig. 4 Synthesis of different forms of lead chalcogenides using $(Me_3Si)_2E$ as chalcogen reagents. Reproduced with permission from ref. 85–89 and 96. Copyright (2014, 2016, 2018) American Chemical Society and (2010) The Royal Society of Chemistry.

When the quantity of $(Me_3Si)_2S$ is less than that of the lead precursor, usually lead oleate produced *in situ* by the reaction of lead oxide and oleic acid (OA), the produced PbS QDs are Pb-rich with the excess of lead precursor located on the surface of the QDs and passivated by the oleic acid, leading to a stable colloidal solution.[81,82] In contrast, noncolloidal aggregated suspensions of PbS NPs are formed on using an excess of $(Me_3Si)_2S$, which removes the oleic acid ligands from the surface of the particles and sulfurizes the surface.[85] These S^{2-} anions on the surface of QDs bind with the Pb atoms of adjacent QDs, thus decreasing the inter-QD spacing drastically inside the spin-coated films, leading to complete disappearance of the exciton absorption peak (Fig. 4b).

On using $(Me_3Si)_2Se$, the selenization of the QDs was also possible (*i.e.* the presence of Se^{2-} instead of S^{2-} on the surface) as confirmed by the red-shift of the absorption onset in the selenized QDs with respect to the sulfurized dots. This is in accordance with the narrower bandgap of PbSe as compared to PbS. It was noted that a chalcogen-rich termination of the PbS QD surface promoted oxidation and facilitated fusion/necking of neighboring QDs. On using PbX_2 (X = Cl, Br, I) as the Pb precursors, it was possible to produce halide-terminated PbS and PbSe QDs which were air-stable (Fig. 4c).[86,87] This low-temperature synthesis also helps in scaling-up of the products, as demonstrated by Zhang *et al.* in the synthesis of about 47 g of PbS QDs with a clear excitonic absorption peak and good size distribution within a few minutes (Fig. 4d).[86]

By exploiting the relative reaction rates of the chalcogenide precursors $(Me_3Si)_2E$ (E = S, Se, Te), which allow for the homogeneous incorporation of the chalcogenide anions, synthesis and characterization of composition-tunable ternary lead chalcogenide alloys $PbSe_xTe_{1-x}$, PbS_xTe_{1-x}, and PbS_xSe_{1-x} were

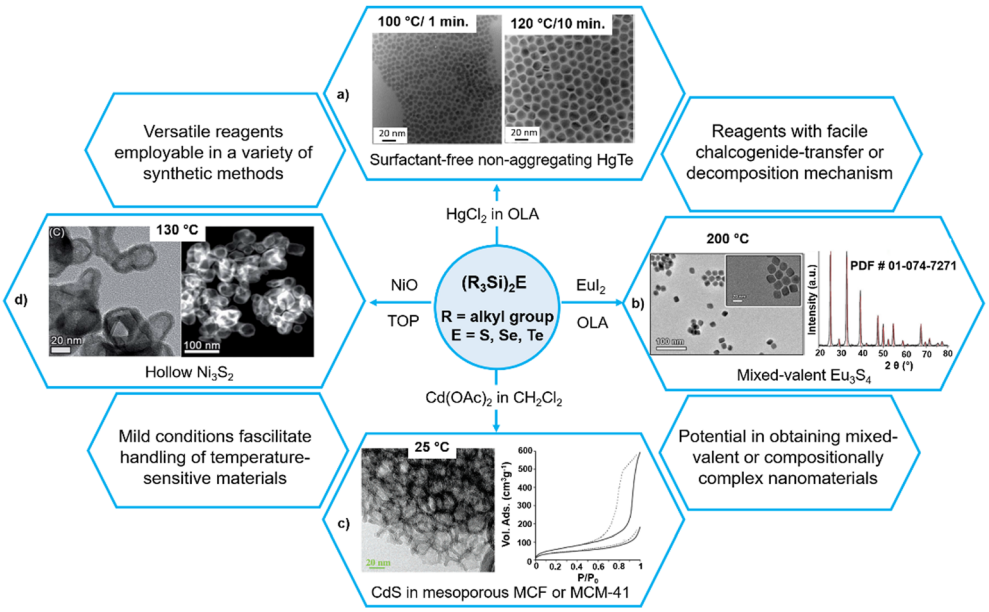

Fig. 5 Versatility of $(Me_3Si)_2E$ in the mild synthesis of different nanoforms of metal chalcogenides. Reproduced with permission from ref. 94, 95, 107 and 113. Copyright (2007, 2017) American Chemical Society; (2017) The Royal Society of Chemistry; and (2021) Wiley-VCH.

reported (Fig. 4e).[92,93] The resulting QDs were Pb-rich but the Pb/anion ratio was size- and composition-dependent and consistent with the reaction rates of the anion precursors.

Without using thiols as stabilizing ligands, Shen *et al.* recently synthesized HgTe colloidal quantum dots with much improved dispersion which can be stored in the cleaned solution for months without any precipitate (Fig. 5a).[94] The authors suggested that the reason behind the colloidal stability was the use of a 2-fold excess of the mercury precursor. As the reaction with highly reactive $(Me_3Si)_2Te$ is quantitative, there is always an excess of Hg precursor which acts as a ligand that binds to the surface Te sites. The high reactivity of $(Me_3Si)_2Te$ ensures a fast growth of the particles and results in spherical quantum dots (QDs), which is in contrast with the strongly faceted HgTe QDs synthesized using TOPTe (where slow growth ensures that slowest growing facets dominate the final structures).

By reacting $(Me_3Si)_2S$ with divalent lanthanide halides LnX_2 (X = Cl, Br, I) in oleylamine, Stoll *et al.* recently synthesized mixed-valent lanthanide sulfide Eu_3S_4 and $EuSm_2S_4$ NPs at 200 °C (Fig. 5b).[95] The authors reported the combination of the high reactivity of $(Me_3Si)_2S$ and the use of low-valent metal halides as a key to stabilize the mixed-valent phases. The fact that only EuI_2 afforded phase-pure Eu_3S_4 (the use of $EuCl_2$ gave EuS NPs, whereas $EuBr_2$ yielded a contaminated sample) highlights the influence of the choice of reagent and the role of kinetics in phase stabilization.

3.1.2. Influence of solvent, reaction time and temperature. The use of olive oil as a solvent and a capping ligand represents a greener and gram scale synthetic route that not only lowers the synthetic temperature to 60 °C but also enhances the air-stability of the NPs (Fig. 4f).[88] The reaction of lead(II) oleate with $(Me_3Si)_2S$ in a mixture of solvents 1,1,2-trichloroethane (1,1,2-TCE) and dimethylformamide (DMF) leads to the formation of PbS nanosheets with lateral dimensions of several hundred nanometers (Fig. 4g).[89] The use of 1,1,2-TCE and DMF was essential for getting nanosheets as only NPs were produced without these two solvents. By varying the reaction temperature and time, the shape and thickness of these nanosheets could be tuned. The stable colloidal suspension of the as-obtained PbS QDs is amenable to further manipulations. For example, these colloidal suspensions could easily be deposited on a glass substrate which, after drying the solvent at different temperatures, resulted in self-organization of the QDs into two- and three-dimensional (3D) superlattices in the form of flakes in parallel orientation to the substrate.[96]

The reaction of $(R_3Si)_2Te$ (R = Me, Et) with GeX_2 (X = chloride, aminoalkoxide) afforded GeTe NPs at low temperatures.[97] Specifically, the reaction of $(Et_3Si)_2Te$ and $GeCl_2$·dioxane was studied in detail. The presence of protic and strongly coordinating primary or secondary amine solvents was essential for the formation of GeTe NPs with defined chemical composition, size, and shape. The nuclear magnetic resonance (NMR) studies revealed that the reaction in oleylamine (OLA) did not proceed with the elimination of Et_3SiCl. Rather, OLA reacted with $(Et_3Si)_2Te$ at ambient temperature with the formation of first silylamine (oleylN(H)$SiEt_3$) and then the $[Te_4]^{2-}$ dianion, which then reacted with $GeCl_2$·dioxane to afford GeTe at temperatures below 150 °C. In contrast, reactions in 1,3-diisopropylbenzene occurred with the elimination of Et_3SiCl and subsequent formation of agglomerated GeTe particles, whereas reactions in tri-*n*-octylamine and 1-hexadecanethiol produced elemental tellurium. In the presence of an excess of $(Et_3Si)_2Te$, GeTe NPs decorated with Te nanowires were obtained. Similarly, the reactions of $(R_3Si)_2E$ (R = Me, Et; E = S, Se, Te) with metal aminoalkoxides of Sb(III) and Bi(III)

at moderate temperatures afforded phase-pure M_2E_3 NPs without any additional elemental or metal-rich phases.[97,98]

Ternary nanoparticles containing two different metals, *i.e.*, $AgSbS_2$ NPs, were synthesized by reacting simultaneously $AgNO_3$ and $SbCl_3$ or [Sb(diethyldithiocarbamate)$_3$] with $(Me_3Si)_2S$ in a mixture of OLA and OA at 180–220 °C.[99] Upon varying the reaction time between 1.5 and 5 minutes, the reaction temperature between 180 and 220 °C or the OLA/OA volume ratio in the range of 4 : 4 to 7.25 : 0.25, a wide range of various sized $AgSbS_2$ NPs with narrow size distributions were obtained in a very precise manner. Similarly, ternary $AgInSe_2$ NPs were synthesized by the hot-injection method by injecting $(Me_3Si)_2Se$ into a solution of AgI and InI_3 in a mixture of OA and TOP at 280 °C.[100] The reaction of $(Me_3Si)_2S$ with $CuIn(OH)_5$ in a mixture of 1-octadecene (ODE), OA and OLA yielded OA-capped $CuInS_2$ NPs at 200 °C, where the use of a bimetallic precursor containing a 1 : 1 ratio of the two metals ensured the desired composition in the synthesized ternary NPs.[101]

3.2. Use of ionic liquids

Ionic liquids offer an interesting synthetic route, not only as effective solvent media, but also as stabilizers and shape-directing templates. Thus, $(Et_3Si)_2Se$ reacted with $SbCl_3$ in $[C_4C_1Im]Cl$ (C_4C_1Im = 1-butyl-3-methylimidazolium) and oleic acid to give phase-pure Sb_2Se_3 at 150 °C as agglomerated nanowires with a high aspect ratio.[102] Similarly, reactions of $(Et_3Si)_2E$ with bismuth-containing ionic liquids $[Cat]_3[Bi_3I_{12}]$ [Cat = C_4C_1Im or C_4mim] in the presence of oleylamine at 150 °C afforded phase-pure Bi_2E_3 (E = Se, Te).[68,102,103] Alternatively, these silylated organyl chalcogenides $(R_3Si)_2E$ can easily be converted to chalcogenide-containing ionic liquids $Cat^+[ESiMe_3]^-$ (Cat^+ = an organic cation) of comparable activity but with higher thermal stability, therefore effectively suppressing the undesired homolytic cleavage of the E–Si bond observed occasionally in the parent $(R_3Si)_2E$.[104] For instance, $[C_4C_1Pyr][ESiMe_3]$ (C_4C_1Pyr = 1-butyl-1-methylpyrrolidinium; E = Se or Te) reacts with bismuth-containing $[C_4C_1Im]_3[Bi_3I_{12}]$ in $[C_4C_1Im]I$ at 150 °C to afford phase-pure Bi_2E_3 free from any elemental Se/Te impurities.[105]

3.3. Sophisticated and intricate multicomponent architectures

One important advantage of the highly reactive nature of these silylated chalcogenides is that they generate metal chalcogenide NPs under mild conditions and therefore can be exploited to generate composites with sensitive materials. For example, these have been employed on a modified mesoporous surface such as Mobil Composition of Matter no. 41 (MCM-41) and mesocellular silica foam (MCF) to form binary CdE and ZnE or ternary $Cd_xZn_{1-x}E$ (E = S, Se, Te) nanomaterials within the host framework at room temperature, and therefore without modifying its mesoporous characteristics (Fig. 5c).[106,107] Even though the surface area of the host matrix after loading with NPs diminishes, it still remains sufficiently high (*e.g.*, 250 $m^2\ g^{-1}$ in CdE loaded MCF against 715 $m^2\ g^{-1}$ in MCF). More importantly, the resulting materials maintain their mesoporosity, indicating their suitability for many applications.

These synthons have also been employed to get sophisticated core@shell structures. For example, the reaction of the pre-formed $Cu_{2-x}Se$ NPs with $ZnEt_2$ and $(Me_3Si)_2S$ in a mixture of OLA and trioctylphosphine oxide (TOPO) afforded core@shell $Cu_{2-x}Se$@ZnS NPs at 175 °C.[108] Similarly, the reaction of ZnO tripods with $(Me_3Si)_2S$ in TOP/TOPO at 250 °C yielded hollow ZnS tripods which on partial cation exchange with Cd^{2+} at 220 °C afforded ZnS@CdS core–shell tripod heterostructures.[109]

3.4. Miscellaneous methods

As said earlier, these ligands can react with non-conventional reagents under a variety of conditions. For instance, using the microemulsion method, nanocrystalline Bi_2Te_3 with particle sizes less than 10 nm were synthesized from the reaction of $BiO(ClO_4)$ with $(Me_3Si)_2Te$ in a reverse micelle formed by sodium dioctyl sulfosuccinate and water in hexane in 70% yield.[110] Similarly, these ligands can also react with pre-formed metallic or metal oxide nanoparticles. For example, $(Me_3Si)_2Te$ reacts with pre-formed colloidal metal nanoparticles of Pd, Pt and Ni under sufficiently mild conditions (180 °C, 1 h) to form their corresponding ditellurides $PdTe_2$, $PtTe_2$, and $NiTe_2$.[111] Other metal nanoparticles of Co, Ag, and Rh also form crystalline metal tellurides upon reaction with $(Me_3Si)_2Te$, indicating that this approach to synthesizing nanoscale transition metal tellurides is general. Interestingly, the reactions of $(Me_3Si)_2E$ with pre-formed nanocrystalline metal oxides (CdO, ZnO, NiO, Co_3O_4 and CoO) at 135–235 °C in TOP/TOPO resulted in nanocrystalline metal chalcogenides (CdS, ZnS, Ni_3S_2, Ni_5Se_5, Co_9S_8 and Co_3Se_4) with hollow, vesicle-like morphologies, as confirmed by transmission electron microscopy (TEM) and high-angle annular dark-field scanning transmission electron microscopy (HAADF-STEM) images (Fig. 5d).[108,112,113] The shape, single crystallinity, and orientation of the parent metal oxide NPs are completely preserved in the transformed particles. The authors explained the hollow morphologies on the basis of a nanoscale Kirkendall-type effect, arising from differential ion diffusion rates between ions in the reactant and product phases. All nanocrystalline chalcogenides produced were surrounded by an outer amorphous silica layer, which could help in preventing agglomeration and degradation. These organyl chalcogenides can also react with more complex precursors such as mixed-metal oxides to yield ternary metal chalcogenide NPs as demonstrated by the reaction of $NiCo_2O_4$ with $(Me_3Si)_2S$ which generated NPs of heterobimetallic $(Ni/Co)_9S_8$ without significant phase segregation.[113] Table 3 summarizes some selected examples of metal chalcogenide nanomaterials synthesized under mild conditions using silylated organyl chalcogenides.

4. Diorganyl dichalcogenides

Since their first use in the synthesis of SnSe and SnTe nanoparticles in 2002,[114] diorganyl dichalcogenides R_2E_2 have emerged as facile chalcogenide reagents in the synthesis of

Table 3 Some selected examples of metal chalcogenide nanomaterials synthesized under mild conditions using $(Me_3Si)_2E$

Reagents/precursors	Materials	Synthesis (temp., solvent, capping ligand, *etc.*)	Ref.	Comments
Binary metal chalcogenides				
$Pb(oleate)_2$ in excess + $(Me_3Si)_2S$	Pb-Rich PbS QDs	115 °C, OA, ODE	81 and 82	Stable colloidal solution due to the presence of oleic acid-protected lead ions on the surface of QDs
PbI_2 + $(Me_3Si)_2E$ in excess	E-Stabilized PbS NPs (E = S, Se)	125 °C, DMF, OA, ODE, OLA	85	The E^{2-} anions on the surface of QDs bind with the Pb atoms of adjacent QDs, which decrease the inter-QD spacing and lead to complete disappearance of the exciton absorption peak
PbX_2 (X = Cl, Br, I) + $(Me_3Si)_2E$	Halide-stabilized and air-stable PbE (E = S, Se) QDs	100–140 °C, OLA	86 and 87	Facile scaled-up synthesis (~47 g of high-quality PbS QDs within a few min)
$Pb(oleate)_2$ + $(Me_3Si)_2S$	Olive oil-stabilized PbS NPs	60 °C, olive oil, OA, ODE	88	Use of olive oil as a green solvent lowers further the synthetic temp. and makes NPs more air-stable
$Pb(oleate)_2$ + $(Me_3Si)_2S$	PbS nanosheets	90 °C, Ph_2O, TOP, 1,1,2-TCE, DMF	89	Use of 1,1,2-TCE and DMF essential for getting nanosheets
$GeCl_2$·dioxane + $(Et_3Si)_2Te$	GeTe NPs	160 °C, OLA	97	Oleylamine essential for the formation of GeTe NPs with defined chemical composition, size, and shape
$M(dmea)_3$ (M = Sb, Bi) + $(R_3Si)_2E$ (R = Me, Et; E = S, Se, Te)	M_2E_3 NPs (M = Sb, Bi)	120-140 °C, DIPB	98	Thermally stable but chemically reactive metal aminoalkoxides lead to phase-pure Bi_2Te_3 without any Bi impurity
$BiO(ClO_4)$ + $(Me_3Si)_2Te$	Bi_2Te_3 NPs	RT, reverse micelles in AOT, H_2O and hexane	110	The microemulsion method facilitates RT synthesis of monodisperse, sub-10 nm NPs
$SbCl_3$ + $(Et_3Si)_2Se$	Sb_2Se_3 nanowires	150 °C, OLA, $[C_4C_1Im]Cl$	102	Reaction easily scalable up to 10 g of NPs
$(Et_3Si)_2E$ + $[C_4C_1Im]_3$-$[Bi_3I_{12}]$ or $[C_4mim]_3[Bi_3I_{12}]$	Bi_2E_3 (E = Se, Te)	150 °C, OLA, $[C_4C_1Im]Cl$ or $[C_4mim]I$	68, 102 and 103	Oleylamine effectively suppresses the homolytic Se–Si bond cleavage to afford the phase-pure product
$Zn(OAc)_2(3,5\text{-}Me_2Py)_2$ + $(Me_3Si)_2E$ (E = S, Se, Te) + MCM-41	ZnE NPs (E = S, Se, Te) within MCM-41	RT, toluene, CH_2Cl_2	106	RT synthesis ensures no modification of the mesoporous characteristics of MCM-41
$Cd(OAc)_2(P^nBu_3)_2$ + $(Me_3Si)_2E$ (E = S, Se, Te) + MCM-41/MCF	CdE (E = S, Se, Te) within the mesoporous hosts	RT, CH_2Cl_2	107	The organic ligand, which anchors the CdE material within MCM-41/MCF, is cleaved on heating beyond 135 °C, resulting in the aggregation of CdE outside of the pores
$HgCl_2$ in excess + $(Me_3Si)_2Te$	Non-aggregating HgTe QDs	100–120 °C, OLA	94	Use of an excess of $HgCl_2$ ensures a well-dispersed and stable colloidal suspension
$EuCl_2$ + $(Me_3Si)_2S$	EuS NPs	200 °C, OLA	95	—
EuI_2 + $(Me_3Si)_2S$	Mixed-valent Eu_3S_4	200 °C, OLA	95	Initially Eu S is formed at lower temperatures, which is converted to Eu_3S_4 over time
SmI_2 + $(Me_3Si)_2S$	Mixed-valent Sm_3S_4	300 °C, OLA	95	Higher reaction temperature due to the greater redox potential of samarium
EuI_2 + SmI_2 + $(Me_3Si)_2S$	Mixed-valent $EuSm_2S_4$	300 °C, OLA	95	Based on XPS, the authors described the materials as $(Eu^{2+})(Eu^{3+},Sm^{3+})_2S_4$
(NHC)MBr (M = Cu, Ag) + $(Me_3Si)_2S$	NHC-protected $Cu_{2-x}S$ or Ag_2S QDs	RT, CH_2Cl_2, ODE	80	Formation of NHC–Ag_2S QDs *via* the intermediate complex [NHC–AgSAg–NHC]
(NHC)MBr (M = Cu, Ag) + $(^tBuMe_2Si)_2Se$	NHC-protected $Cu_{2-x}Se$ or Ag_2Se QDs	RT, CH_2Cl_2, THF	80	NHC ligands containing long carbon chains have superior competence over commonly used organic capping ligands (OA, OLA) for obtaining highly monodisperse QDs
Metal NPs (Pd, Pt, Ni) + $(Me_3Si)_2Te$	MTe_2 NPs (M = Pd, Pt, Ni)	180 °C, TOPO, OLA	111	The high reactivity of silylated $(Me_3Si)_2Te$ ensures formation of the telluride-rich phase MTe_2 over MTe
$(Me_3Si)_2S$ + ZnO NPs	ZnS NPs with hollow morphology	235 °C, TOP/TOPO	112	The tetrapod morphology of ZnO is preserved in ZnS
$(Me_3Si)_2S$ + CdO NPs	CdS NPs with hollow morphology	130 °C, TOP/TOPO	109	The pseudo-spherical shape and crystallinity of CdO are preserved in the CdS NPs
$(Me_3Si)_2E$ (E = S, Se) + NiO NPs	Ni_3S_2 or Ni_5Se_5 NPs with hollow morphology	130 °C, TOP	113	Silylated organyl chalcogenides generate a protecting amorphous silica layer around NPs
Co_3O_4 or CoO NPs + $(Me_3Si)_2E$ (E = S, Se)	Co_9S_8 or Co_3Se_4 NPs with hollow morphology	130 °C, TOP	113	Hollow morphologies due to the nanoscale Kirkendall-type effect arising from different ion diffusion rates
$Cu(TFA)_2$ + $(Me_3Si)_2S$	ODT-capped CuS NPs	RT, ODT, Et_2O	43	The high reactivity of $(Me_3Si)_2S$ ensures the formation of phase-pure CuS in 90% yield
Ag(TFA) + $(Me_3Si)_2S$	ODT-capped Ag_2S NPs	RT, ODT, Et_2O	43	Instant formation of phase-pure Ag_2S in 95% yield
Ternary metal chalcogenides				
$Pb(oleate)_2$ + $(Me_3Si)_2E$ (E = S, Se, Te)	$PbSe_xTe_{1-x}$, PbS_xTe_{1-x}, and PbS_xSe_{1-x}	140 °C, OA and ODA	92	Composition-tunable ternary alloys due to excellent compatibility among $(Me_3Si)_2E$

Table 3 (*continued*)

Reagents/precursors	Materials	Synthesis (temp., solvent, capping ligand, *etc.*)	Ref.	Comments
$Pb(oleate)_2$ + $(Me_3Si)_2S$ + $(Me_3Si)_2Se$	PbS_xSe_{1-x} (x = 0.2–0.8)	130 °C, olive oil, ODA	93	Comparable reactivities of $(Me_3Si)_2S$ and $(Me_3Si)_2Se$ allow homogeneous incorporation of the chalcogenide anions
$AgNO_3$ + $SbCl_3$ + $(Me_3Si)_2S$	$AgSbS_2$ NPs	180–220 °C, OLA, OA	99	Various sized $AgSbS_2$ NPs with narrow size distributions as a function of reaction conditions (time, temp. or the OLA/OA volume)
$(Me_3Si)_2S$ + $NiCo_2O_4$ NPs	$(Ni/Co)_9S_8$ NPs with hollow morphologies	130 °C, TOP	113	High reactivity of silylated $(Me_3Si)_2S$ ensures no significant phase segregation
$CuIn(OH)_5$ +$(Me_3Si)_2S$	OA-Capped $CuInS_2$ NPs	200 °C, ODE, OA, OLA	101	NPs remain well-dispersed in non-polar solvents for several months
$Cu_{2-x}Se$ NPs + $ZnEt_2$ + $(Me_3Si)_2S$	Core@shell Cu_{2-x}-Se@ZnS NPs	175 °C, OLA, TOPO	108	Stable plasmonic behavior by the core–shell structure

Abbreviations: AOT = sodium dioctyl sulfosuccinate; C_4C_1Im = 1-butyl-3-methylimidazolium; DIPB = 1,3-diisopropylbenzene; dmea = 1,1-dimethylethanolamine; DMF = dimethylformamide; OA = oleic acid; ODE = 1-octadecene; ODT = octadecane thiol; OLA = oleylamine; TOP = trioctylphosphine; TOPO = trioctylphosphine oxide; MW = microwave; RT = room temperature; NHC = N-heterocyclic carbene; NPs = nanoparticles; QDs = quantum dots.

binary, ternary and multinary metal chalcogenide NPs of controlled size and shape.[26,27]

4.1. A comparison with diorganyl monochalcogenides

These reagents enjoy mostly the same advantages described above for the R_2E reagents, *i.e.* easy tunability of reactivity by varying the group R, facile transfer of the chalcogenide anion under mild conditions, easily removable byproducts, good solubility in common organic solvents, *etc.* However, these diorganyl dichalcogenides R_2E_2 do have an additional E–E bond which is cleaved rather easily under mild conditions. As a result, they rarely act as neutral ligands towards metal centres and, unlike a rich library available of metal complexes with organyl monochalcogenides,[32,33] there are very few metal complexes reported so far with neutral R_2E_2 ligands, mostly isolated at a low temperature.[115,116] However, these complexes are not stable and quickly decompose to give monochalcogenide complexes.[115,116] While the presence of an additional E–E bond alters the decomposition pathways of R_2E_2 and makes them slightly less reactive than R_2E reagents, it also renders them more air- and temperature-stable, resulting in easy handling and more commercial availability of a wide variety of differently substituted diorganyl dichalcogenides R_2E_2 (where E = S, Se, or Te and R = alkyl, allyl, benzyl, or aryl).[25–27] Another advantage of these reagents is that they can easily be transformed *in situ* to monoalkyl chalcogenides R–E *via* E–E cleavage, which can act as capping ligands to stabilize the formed NPs. This has implications in the chemistry of RSe- and RTe-stabilized NPs as, unlike thiol ligands, which have been extensively employed as surfactant for semiconducting NPs, the selenol and tellurol ligands are usually oxidatively instable and hence are difficult to use.[26] With an exception of a couple of reports,[117,118] the diorganyl dichalcogenides employed so far in the synthesis of metal chalcogenides are almost entirely non-silylated. This is in contrast to diorganyl monochalcogenides where silylated derivatives form the bulk of the reported examples.

The decomposition of R_2E_2, either thermally[25–27] or photolytically,[119,120] proceeds through the radical scission of the E–E and E–C bonds. The mechanism has been studied in detail by Vela *et al.* who carried out a combined experimental and DFT study correlating the bond strengths in R_2E_2 with the size and shape of the obtained CdSe and CdS NPs.[25] They demonstrated that, by changing the R group within the series of R_2E_2 (E = S, Se), the reactivities of these chalcogenide reagents could be tuned. While the E–E bond strength was found to be relatively constant, the calculated C–E bond strengths changed significantly upon substituting the R group and determined the

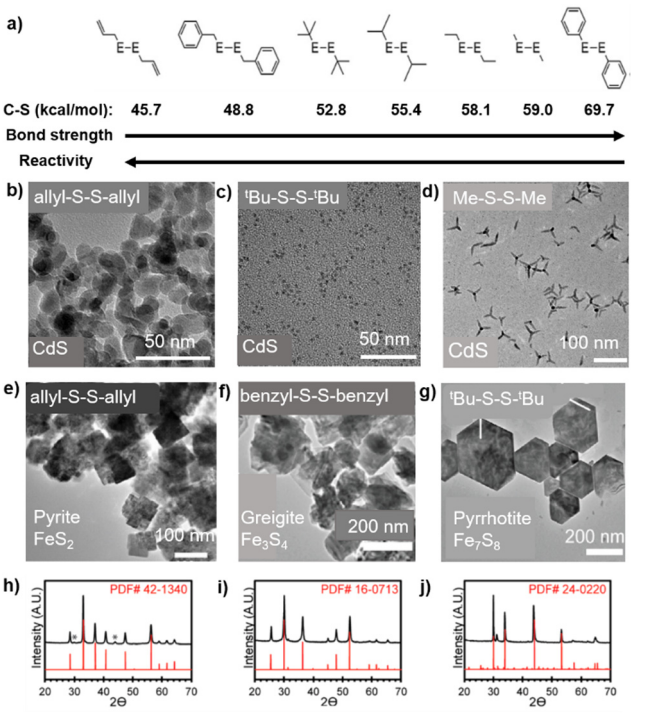

Fig. 6 Varying C–S bond strengths and reactivities among R_2E_2 precursors (a) and its influence on the particle shape (b–d) as well as composition and crystalline phase (e–j) of metal chalcogenide nanomaterials. Adapted with permission from ref. 25 and 27. Copyright (2013, 2017) American Chemical Society.

Table 4 Some selected examples of metal chalcogenide nanomaterials synthesized under mild conditions using R_2E_2

Reagents	Materials	Synthesis (temp., solvent, capping ligand, *etc.*)	Ref.	Comments
Ph_3Bi + $^tBu_2Se_2$	BiSe NPs	RT photolysis (254 nm per 4 h), DDA, P-123 copolymer	120	Ph_3Bi and $^tBu_2Se_2$ both undergo homolytic photolysis without using a reducing reagent to produce 5 nm BiSe NPs
GeI_4 + Ph_2Se_2	GeSe nanosheets	268 °C, HDA	121	—
Metallic Sn NPs + Ph_2Te_2	Surfactant-free SnTe NPs	165 °C, diglyme	114	Large spherical NPs (~60 nm) or smaller star-shaped agglomerates of needles (~15 × 40 nm) are obtained depending on the Sn/Ph_2Te_2 ratio
$SnCl_2$ + $^tBu_2Se_2$	SnSe NPs	180 °C, DDA, DDT	122	Stoichiometric $SnCl_2$/$^tBu_2Se_2$ ratio yielded phase-pure SnSe, whereas an excess of $^tBu_2Se_2$ yielded $SnSe_2$
SnI_4 + GeI_4 + $^tBu_2Se_2$	Ternary $Sn_xGe_{1-x}Se$ NPs	225 °C, DDA, HMDS	123	In the absence of HMDS, only binary SnSe NPs were produced
CuCl + SnI_4 + $^tBu_2Se_2$	Wurtzite Cu_2SnSe_3 NPs	180 °C, DDA, DDT	42	The combination of DDT and $^tBu_2Se_2$ is critical to obtain the wurtzite phase of Cu_2SnSe_3
$In(acac)_3$ + $^tBu_2S_2$	In_2S_3 nanorods	180 °C, OLA	124	Synthesis of In_2S_3 nanorods takes 7 h due to the less reactivity of $^tBu_2S_2$
CuCl + $In(acac)_3$ + $^tBu_2S_2$	Wurtzite Cu–In–S NPs	180 °C, OLA, DDT	125	Slow formation of In_2S_3 leads to the isolation of a metastable wurtzite Cu–In–S phase
$Cu(oleate)_2$ + Ph_2Se_2	Wurtzite-like $CuInSe_2$ NPs	220 °C, OLA	49	The metastable phase is formed through the Cu_3Se_2 intermediate
$InCl_3$ + $SnCl_2$ + Ph_2Se_2	In_4SnSe_4 microwires	280 °C, HMDS, OLA, ODE	126	—
ZnO + $^tBu_2S_2$	ZnS NPs	235 °C, OLA, TOP	127	ZnS with a hollow structure, induced by the nanoscale Kirkendall effect
$Cd(oleate)_2$ + R_2E_2 (R = allyl, Bz, *t*Bu, iPr, Et, Me, Ph; E = S or Se)	CdS and CdSe NPs	250 °C, OLA, OA, ODE	25	CdS and CdSe NPs with spherical, elongated or tetrapodal morphology by varying the reactivity of R_2E_2
$CuCl_2$ + $^tBu_2S_2$	$Cu_{2-x}S$ NPs	180-220 °C, OLA + DDT	128	Roxbyite $Cu_{1.78}S$ or Djurleite $Cu_{1.96}S$ depending on Cu concentration
$Cu(acac)_2$ + $(dodecyl)_2Se_2$	Wurtzite $Cu_{2-x}Se$ NPs	155 °C, ODE	50	Metastable wurtzite $Cu_{2-x}Se$ NPs are irreversibly transformed to thermodynamic cubic Cu_2Se at 185 °C
$Cu(oleate)_2$ + Ph_2Se_2	Wurtzite Cu_3Se_2 NPs	220 °C, OLA	49	Metastable wurtzite Cu_3Se_2 NPs
$Cu(acac)_2$ + $(dodecyl)_2Te_2$	Pseudo-cubic $Cu_{1.5}Te$ NPs	135 °C in a variety of solvents (ODE, OlA, OA and DOE)	51	Metastable pseudo-cubic $Cu_{1.5}Te$ NPs are formed at 135 °C, whereas a thermodynamic vulcanite CuTe phase is obtained at 185 °C
$Cu(oleate)_2$ + Ph_2Se_2 + $Zn(oleate)_2$ + $Fe(acac)_3$	Wurtzite-like $Cu_2FeSnSe_4$ NPs	250 °C, OLA	129	Metastable quaternary NPs through sequential cationic replacement in the initially formed binary Cu_3Se_2 NPs
$Cu(oleate)_2$ + Ph_2Se_2 + $Zn(oleate)_2$ + Sn(ethylhexanoate)$_2$	Wurtzite-like $Cu_2ZnSnSe_4$ NPs	255 °C, OLA	130	Metastable quaternary NPs through sequential cationic replacement in the initially formed binary Cu_3Se_2 NPs
$AgNO_3$ + $In(OAc)_3$ + Bz_2Se_2	Metastable $AgInSe_2$ NPs	230 °C, OLA, OA, ODE	131	Presence of oleylamine essential to get the metastable phase
CuCl + $Fe(acac)_3$ + Ph_2Se_2	$CuFeSe_2$ nanosheets	255 °C, OA, OLA, ODE	132	Hierarchical nanostructures assembled from nanosheets of ~50 nm thickness and ~400 nm side length
$FeCl_2$ + $(allyl)_2S_2$	Pyrite FeS_2 NPs	220 °C, OLA	27	Due to a lower C–S bond energy as compared to the S–S one, $(allyl)_2S_2$ releases a persulfide $(S–S)^{2-}$ ion, leading to formation of pyrite FeS_2 NPs
$FeCl_2$ + $(benzyl)_2S_2$	Greigite Fe_3S_4 NPs	220 °C, OLA	27	A sulphur-deficient phase is obtained through the rupture of the S–S bond
$FeCl_2$ + R_2S_2 (R = ^{t}Bu, Ph)	Pyrrhotite Fe_7S_8 NPs	220 °C, OLA	27	A sulphur-deficient phase is obtained through the rupture of the S–S bond
WCl_4 + $^tBu_2Se_2$	Amine-stabilized WSe_2 nanosheets	225 °C, DDA	133	Addition of tetra-*n*-octylammonium bromide prevents agglomeration of colloidal 2H-WSe_2 nanosheets
$W(CO)_6$ + Ph_2Se_2	WSe_2 NPs	330 °C, OA, TOPO	134	A higher OA/$W(CO)_6$ molar ratio yields slower nucleation, larger NPs and a shift from the 2H to the 1T' crystal phase
$W(CO)_6$ + Ph_2Se_2	MSe_2 (M = Mo, W) nanosheets	330 or 350 °C, OA, OLA, oleyl alcohol	135	Single-layer MSe_2 nanosheets obtained by using oleic acid, while multilayer nanosheets are formed with oleyl alcohol and oleylamine
$MoCl_5$ + WCl_6 + Ph_2Se_2	$Mo_xW_{1-x}Se$	300 °C, OA, OLA, HMDS	136	Easily tunable compositions by varying the Mo and W ratio

Abbreviations: DDA = dodecylamine; HAD = hexadecylamine; DDT = dodecanethiol; HMDS = hexamethyldisilazane $(Me_3Si)_2NH$; OA = oleic acid; ODE = 1-octadecene; ODT = octadecane thiol; OLA = oleylamine; TOP = trioctylphosphine; TOPO = trioctylphosphine oxide; RT = room temperature; NPs = nanoparticles.

overall reactivity of the R_2E_2. As compared to the R_2E_2 with weaker C–E bonds which were reactive and afforded isotropic NPs, those with large C–E bond dissociation energies were less reactive and yielded anisotropic, and often morphologically metastable NPs with higher surface areas (Fig. 6). Interestingly, the strength of the C–Se bond not only influences the kinetics of R_2E_2, but also determines the nature of the crystalline phase and composition of the product. For instance, the reactions of diallyl disulfide [$(allyl)_2S_2$] and dibenzyl disulfide with $FeCl_2$ in oleylamine at 220 °C yielded the pyrite (FeS_2) and greigite (Fe_3S_4) phases, respectively, whereas the reactions of di-*tert*-butyl disulfide $^tBu_2S_2$ and di-phenyl disulfide (Ph_2S_2) under similar conditions produced the pyrrhotite (Fe_7S_8) phase.[27] By exploiting this easy tunability of the reactivities by varying the R group, a number of articles have described the use of differently substituted R_2E_2 in the synthesis of binary, ternary or even multinary metal chalcogenide NPs in the last ten years. Some selected examples are summarized in Table 4.

The different reactivities of diorganyl mono- and dichalcogenides can be highlighted by comparing the reactions of $^tBu_2E$ and $^tBu_2E_2$. As compared to $^tBu_2E$ which often affords molecular precursors with low decomposition temperature (Fig. 1) or even NPs at room temperature (Fig. 2), the reaction of $^tBu_2E_2$ requires relatively high temperature to afford NPs of binary and ternary metal chalcogenide NPs (Fig. 7). For instance, $^tBu_2Se_2$ reacts with $SnCl_2$ or a combination of CuCl and SnI_4 to yield binary SnSe and ternary Cu_2SnSe_3 NPs, respectively, at 180 °C in the presence of dodecylamine (DDA) and dodecanethiol (DDT) (Fig. 7a and b).[42,122] While the stoichiometric ratio of Sn and Se reagents was essential for getting phase-pure SnSe NPs, the use of DDT and hexamethyldisilazane (HMDS) was critical to obtain the new wurtzite phase of Cu_2SnSe_3 NPs. Similarly, ternary $Sn_xGe_{1-x}Se$ NPs were prepared by reacting $^tBu_2Se_2$ with varying ratios of GeI_4 and SnI_4 in DDA and HMDS at 225 °C.[123] The decomposition of $^tBu_2E_2$ (E = Se, Te) can be triggered photolytically also, thus decreasing the reaction temperature significantly.[119,120] For example, the photolytic decomposition at 254 nm for 4 h of the deaerated solution of Ph_3Bi and $^tBu_2Se_2$ in water containing dodecylamine and a triblock copolymer P-123 yielded BiSe NPs of an average size of 5 nm (Fig. 7c).[120] As observed in the case of the R_2E series, a stronger C–S bond (in comparison to the C–Se bond) makes R_2S_2 slightly less reactive. For example, the reaction of $CuCl_2$ with an excess of $^tBu_2S_2$ yields roxbyite $Cu_{2-x}S$ NPs, where a slow but continuous growth of the nanoparticles (due to the low nucleation rate of the reagent) not only ensured accurate size control of the NPs but also allowed to follow their gradual morphology evolution from spheres and disks to tetradecahedrons and dodecahedrons (Fig. 7d).[128] The relatively slow reactivity of $^tBu_2S_2$ is further manifested from its reaction with $In(acac)_3$ which required 7 h to afford In_2S_3 at 180 °C (Fig. 7e).[124] This slow rate was subsequently exploited to synthesize metastable

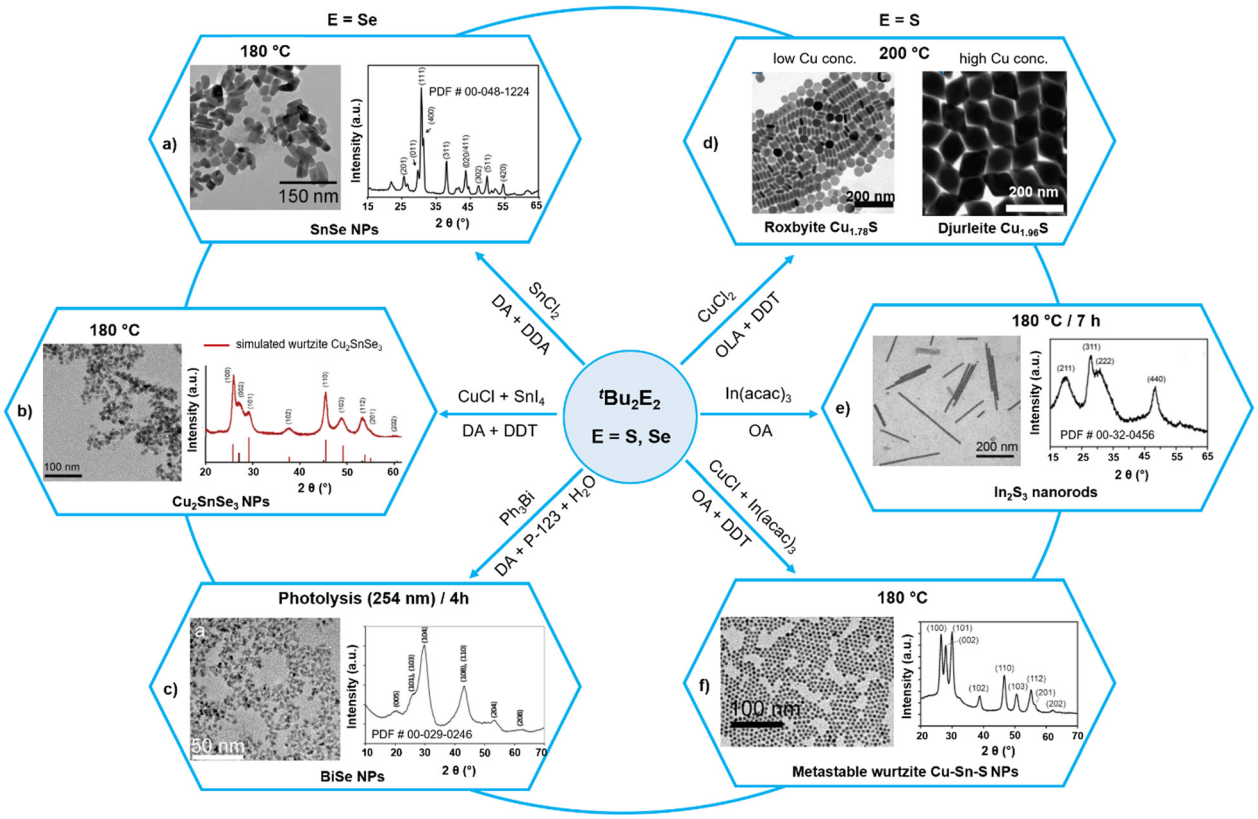

Fig. 7 Utilization of $^tBu_2E_2$ (E = S, Se) precursors to get binary and ternary metal chalcogenide nanoparticles. Adapted with permission from ref. 42, 120, 122, 124, 125, and 128. Copyright (2011) The Royal Society of Chemistry and (2009, 2009, 2010, 2011, 2012) American Chemical Society.

wurtzite ternary CuInS NPs by performing the above reaction in the presence of CuCl and DDT (Fig. 7f).[125] Other sulphur sources such as elemental S_8 or *tert*-butyl thiol produced either no crystalline products or thermodynamic chalcopyrite phase.

4.2. Isolation of metastable phases

While materials in metastable crystal structures can afford useful properties, synthesizing metastable materials necessarily requires kinetic control of the chemistry away from thermodynamic equilibrium, which is not always easy to achieve. The above results showed that variable reactivity in the R_2E_2 series, obtained simply by changing the R and E, could be utilized to control the reaction kinetics and hence predict and provide the synthetic pathways for thermodynamically or kinetically driven products. Unsurprisingly, these reagents have been employed prominently in the past few years for the synthesis and isolation of several metastable phases (Fig. 8). For instance, the reactions of $Cu(acac)_2$ with $(dodecyl)_2E_2$ (E = Se, Te) in a variety of solvents (ODE, OlAm, OA or DOE) afforded metastable wurtzite $Cu_{2-x}Se$ and pseudo-cubic $Cu_{1.5}Te$ NPs at 155 and 135 °C, respectively.[50,51] The right choice of the organyl group in R_2E_2 was important for isolating these metastable phases under mild synthetic conditions because at higher temperature (185 °C) these phases are irreversibly transformed into the thermodynamic cubic Cu_2Se and vulcanite CuTe phases, respectively. Similarly, using Ph_2Se_2 that possesses a higher C-Se bond strength, a "wurtzite-like" metastable phase of the ternary $CuInSe_2$ was obtained, whereas R_2Se_2 (R = methyl, benzyl) with weaker C–Se bonds yielded NPs with the thermodynamic chalcopyrite crystal structure.[49] These two phases are formed *via* distinct copper selenide intermediates, with the wurtzite-like phase forming through Cu_3Se_2 and the chalcopyrite forming through $Cu_{2-x}Se$ intermediates.

The fact that the reaction of Ph_2Se_2 with $Cu(oleate)_2$ in oleylamine yields preferentially the metastable Cu_3Se_2 intermediate which possesses a pseudo-hexagonal selenium sublattice that serves as a template for the ultimate wurtzite-like products has been exploited further to isolate many metastable phases. Thus, wurtzite-like metastable multinary $Cu_2FeSnSe_4$ and $Cu_2ZnSnSe_4$ have been isolated by *in situ* sequential cation exchange reactions between the intermediate Cu_3Se_2 NPs and metal precursors in solution.[128,129] Besides the reactivity of the R_2E_2 reagent, the choice of surfactants employed also influences the course of the reaction and the nature of the final products. This is demonstrated by the reaction of Bz_2Se_2 with $AgNO_3$ and $In(OAc)_3$ in the presence of either oleic acid or oleylamine, which yielded thermodynamic chalcopyrite and metastable orthorhombic phases, respectively, of the ternary $AgInSe_2$ NPs at 250 °C.[130] The authors explained it on the basis of the tetragonal-to-orthorhombic phase transformation of the intermediate Ag_2Se in the presence of oleylamine, which is then converted to the metastable orthorhombic phase of $AgInSe_2$ *via* fast In^{3+} cation exchange due to structural similarities between the two phases. In the absence of oleylamine, the Ag_2Se intermediate is converted to the thermodynamic chalcopyrite structure of $AgInSe_2$ *via* kinetically slow nontopotactic conversion

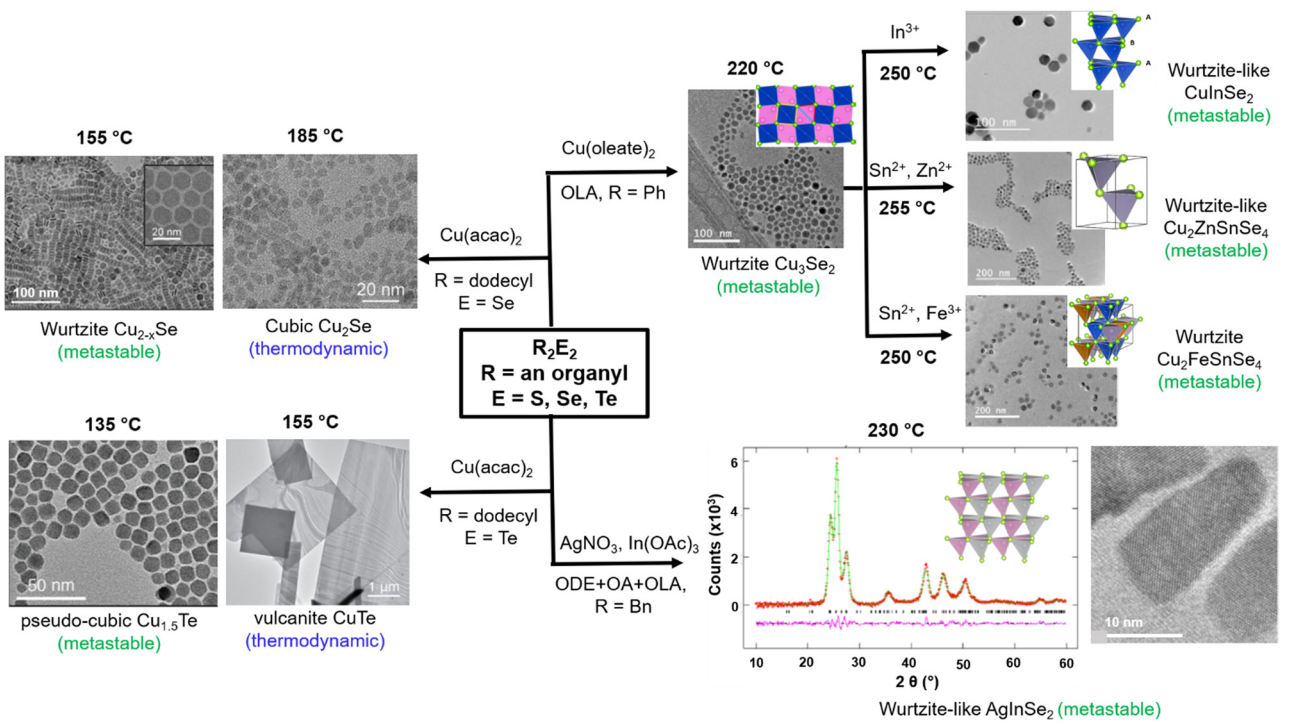

Fig. 8 Isolation of metastable phases of binary and ternary metal chalcogenide NPs using R_2E_2 (R = an organyl; E = S, Se, Te) precursors. Images reproduced with permission from ref. 49–51 and 129–131. Copyright (2020) The Royal Society of Chemistry and (2018, 2019, 2020, 2021, 2021) American Chemical Society.

processes due to structural dissimilarities between the intermediate Ag_2Se and chalcopyrite $AgInSe_2$.

5. Conclusions and looking ahead

This feature article provides a concise and comparative overview on the chemistry and reactivity of three related families of organyl chalcogenides as convenient reagents for the ultra-mild synthesis of metal chalcogenide nanomaterials. These synthons not only transfer the chalcogenide anion (E^{2-}) to a metal center under mild conditions but also allow their reactivity and properties to be modulated. Furthermore, their commercial availability, high solubility in common organic solvents and ability to react in a facile manner even with non-conventional metal reagents make them ideal precursors for scaled-up and controlled synthesis of nanometric metal chalcogenides.

Unlike diorganyl dichalcogenides R_2E_2, the solution-phase utilization of diorganyl monochalcogenides has mostly been restricted to the silylated derivatives $(R_3Si)_2E$. Recent employment of nonsilylated diorganyl monochalcogenides R_2E, which are less reactive than their silylated counterparts, has allowed the isolation and characterization of reactive molecular intermediates containing coinage metals during the synthesis of metal chalcogenides. An extension of this chemistry to other metals would help develop a broader understanding of the molecule-to-nanoparticle transformation and, therefore, achieve the synthesis of even compositionally complex materials with greater control. Recent work indicates that, by using non-silylated R_2E, especially the ones that have a facile decomposition mechanism, it should also be possible to prepare a library of precursors that decompose at very low temperature to generate metal chalcogenide nanomaterials under ultra-mild conditions.[43–46] These studies should be extended to the heterometallic complexes $[M_xM'_y(R_2E)_z]$ containing two different metals or heteroleptic complexes $[M_x(R_2E)_y(R_2E')_z]$ with two different organyl chalcogenide ligands. These single source precursors with enhanced properties can overcome the problem of controlling the stoichiometry of the constituent elements, which often hinders the reproducibility in the synthesis of ternary metal chalcogenides. Reagents or precursors having comparable decomposition characteristics can also be a viable option for controlled synthesis of ternary phases, and despite some recent progress in it,[63,92,93] better knowledge is required. A detailed computational and experimental study involving a systematic change of the R group to determine the variable reactivity in non-silylated R_2E reagents would further allow us to control the reaction conditions, particularly to provide new synthetic pathways for kinetically-driven products. Previous studies on the R_2E_2 series have shown that the precursors possessing strong R–E bonds and therefore being less reactive are better suited for getting metastable phases.[49] Non-silylated R_2E, which are less reactive than silylated $(R_3Si)_2E$, have great potential in this regard.

Conflicts of interest

There are no conflicts to declare.

Acknowledgements

The financial support provided by the Université Claude Bernard Lyon 1 and the infrastructural support available at IRCELYON are thankfully acknowledged. The author also thanks his former PhD and master's students who worked in this field and whose names appear in the reference section.

Notes and references

1 X. Chen, J. Yang, T. Wu, L. Li, W. Luo, W. Jianga and L. Wang, *Nanoscale*, 2018, **10**, 5130–15163.
2 C. Coughlan, M. Ibanez, O. Dobrozhan, A. Singh, A. Cabot and K. M. Ryan, *Chem. Rev.*, 2017, **117**, 5865–6109.
3 X. Cao, C. Tan, X. Zhang, W. Zhao and H. Zhang, *Adv. Mater.*, 2016, **28**, 6167–6196.
4 C. Han, Q. Sun, Z. Li and S. X. Dou, *Adv. Energy Mater.*, 2016, **6**, 1600498.
5 L. Polavarapu, S. Mourdikoudis, I. Pastoriza-Santos and J. Perez-Juste, *CrystEngComm*, 2015, **17**, 3727–3762.
6 T. Heine, *Acc. Chem. Res.*, 2015, **48**, 65–72.
7 R. Gui, H. Jin, Z. Wang and L. Tan, *Coord. Chem. Rev.*, 2015, **296**, 91–124.
8 F. C. J. M. van Veggel, *Chem. Mater.*, 2014, **26**, 111–122.
9 S. R. Alvarado, Y. Guo, T. P. A. Ruberu, E. Tavasoli and J. Vela, *Coord. Chem. Rev.*, 2014, **263–264**, 182–196.
10 S. V. Kershaw, A. S. Susha and A. L. Rogach, *Chem. Soc. Rev.*, 2013, **42**, 3033–3087.
11 Y. Shirasaki, G. J. Supran, M. G. Bawendi and V. Bulovic, *Nat. Photonics*, 2013, **7**, 13–23.
12 J. Li and J. J. Zhu, *Analyst*, 2013, **138**, 2506–2515.
13 E. A. Weiss, *Acc. Chem. Res.*, 2013, **46**, 2607–2615.
14 Z. Han, F. Qiu, R. Eisenberg, P. L. Holland and T. D. Krauss, *Science*, 2012, **338**, 1321–1324.
15 G. S. Li, D. Q. Zhang and J. C. Yu, *Environ. Sci. Technol.*, 2009, **43**, 7079–7085.
16 X. Michalet, F. F. Pinaud, L. A. Bentolila, J. M. Tsay, S. Doose, J. J. Li, G. Sundaresan, A. M. Wu, S. S. Gambhir and S. Weiss, *Science*, 2005, **307**, 538–544.
17 C. B. Murray, D. J. Norris and M. G. Bawendi, *J. Am. Chem. Soc.*, 1993, **115**, 8706–8715.
18 M. A. Malik, M. Afzaal and P. O'Brien, *Chem. Rev.*, 2010, **110**, 4417–4446.
19 M. D. Khan, M. A. Malik and N. Revaprasadu, *Coord. Chem. Rev.*, 2019, **388**, 24–47.
20 V. Brune, M. Grosch, R. Weißing, F. Hartl, M. Frank, S. Mishra and S. Mathur, *Dalton Trans.*, 2021, **50**, 12365–12385.
21 C. Glynn and C. O'Dwyer, *Adv. Mater. Interfaces*, 2017, **4**, 1600610.
22 C. Panda, P. W. Menezes and M. Driess, *Angew. Chem., Int. Ed.*, 2018, **57**, 11130–11139.
23 I. Bretos, R. Jimenez, J. Ricote and M. L. Calzada, *Chem. Soc. Rev.*, 2018, **47**, 291–308.
24 S. Mishra and S. Daniele, *Chem. – Eur. J.*, 2020, **26**, 9292–9303.
25 Y. Guo, S. R. Alvarado, J. D. Barclay and J. Vela, *ACS Nano*, 2013, **7**, 3616–3626.
26 R. L. Brutchey, *Acc. Chem. Res.*, 2015, **48**, 2918–2926.
27 J. M. Rhodes, C. A. Jones, L. B. Thal and J. E. Macdonald, *Chem. Mater.*, 2017, **29**, 8521–8530.
28 S. Dehnen, A. Eichhöfer and D. Fenske, *Eur. J. Inorg. Chem.*, 2002, 279–2317.
29 J. F. Corrigan, O. Fuhr and D. Fenske, *Adv. Mater.*, 2009, **21**, 1867–1871.
30 O. Fuhr, S. Dehnen and D. Fenske, *Chem. Soc. Rev.*, 2013, **42**, 1871–1906.
31 D. G. Macdonald and J. F. Corrigan, *Philos. Trans. R. Soc., A*, 2010, **368**, 1455–1472.
32 Y. P. Chang, W. Levason and G. Reid, *Dalton Trans.*, 2016, **45**, 18393–18416.
33 W. Levason, G. Reid and W. Zhang, *Dalton Trans.*, 2011, **40**, 8491–8506.

34 N. D. Boscher, C. J. Carmalt and I. P. Parkin, *J. Mater. Chem.*, 2006, **16**, 122–127.
35 N. D. Boscher, C. J. Carmalt, R. G. Palgrave and I. P. Parkin, *Thin Solid Films*, 2008, **516**, 4750–4757.
36 P. I. Kuznetsov, V. O. Yapaskurt, B. S. Shchamkhalova, V. D. Shcherbakov, G. G. Yakushcheva, V. A. Luzanova and V. A. Jitov, *J. Cryst. Growth*, 2016, **455**, 122–128.
37 B. J. Choi, S. Choi, Y. C. Shin, K. M. Kim, C. S. Hwang, Y. J. Kim, Y. J. Son and S. K. Hong, *Chem. Mater.*, 2007, **19**, 4387–4389.
38 S. L. Benjamin, Y. Chang, C. Gurnani, A. L. Hector, M. Huggon, W. Levason and G. Reid, *Dalton Trans.*, 2014, **43**, 16640–16648.
39 S. L. Benjamin, C. H. (Kees) de Groot, C. Gurnani, A. L. Hector, R. Huang, E. Koukharenko, W. Levason and G. Reid, *J. Mater. Chem. A*, 2014, **2**, 4865–4869.
40 S. L. Benjamin, C. H. (Kees) de Groot, C. Gurnani, S. L. Hawken, A. L. Hector, R. Huang, M. Jura, W. Levason, E. Reid, G. Reid, S. P. Richards and G. B. G. Stenning, *J. Mater. Chem. C*, 2018, **6**, 7734–7739.
41 K. George, C. H. (Kees) de Groot, C. Gurnani, A. L. Hector, R. Huang, M. Jura, W. Levason and G. Reid, *Chem. Mater.*, 2013, **25**, 1829–1836.
42 M. E. Norako, M. J. Greaney and R. L. Brutchey, *J. Am. Chem. Soc.*, 2012, **134**, 23–26.
43 S. Gahlot, B. Purohit, E. Jeanneau and S. Mishra, *Chem. – Eur. J.*, 2021, **27**, 10826–10832.
44 S. Mishra, D. Du, E. Jeanneau, F. Dappozze, C. Guillard, J. Zhang and S. Daniele, *Chem. – Asian J.*, 2016, **11**, 1658–1663.
45 S. Gahlot, E. Jeanneau, F. Dappozze, C. Guillard and S. Mishra, *Dalton Trans.*, 2018, **47**, 8897–8905.
46 S. Gahlot, E. Jeanneau, D. Singh, P. K. Panda, Y. K. Mishra, R. Ahuja, G. Ledoux and S. Mishra, *Inorg. Chem.*, 2020, **59**, 7727–7738.
47 S. Gahlot, F. Dappozze, D. Singh, R. Ahuja, L. Cardenas, L. Burel, D. Amans, C. Guillard and S. Mishra, *Dalton Trans.*, 2020, **49**, 3580–3591.
48 S. Mishra and S. Gahlot, *Nanomaterials via Single-Source Precursors: Synthesis, Processing and Applications*, ed. A. W. Apblett, A. R. Barron and A. F. Hepp, Elsevier, 2022, ch. 6, pp. 201–218.
49 (*a*) B. A. Tappan, G. Barim, J. C. Kwok and R. L. Brutchey, *Chem. Mater.*, 2018, **30**, 5704–5713; (*b*) M. E. Norako and R. L. Brutchey, *Chem. Mater.*, 2010, **22**, 1613–1615.
50 E. A. Hernández-Pagán, E. H. Robinson, A. D. La Croix and J. E. Macdonald, *Chem. Mater.*, 2019, **31**, 4619–4624.
51 E. H. Robinson, K. M. Dwyer, A. C. Koziel, A. Y. Nuriye and J. E. Macdonald, *Nanoscale*, 2020, **12**, 23036–23041.
52 S. Schulz, *Coord. Chem. Rev.*, 2015, **297–298**, 49–76.
53 N. L. Pickett, D. F. Foster, N. Maung and D. J. Cole-Hamilton, *J. Mater. Chem.*, 1999, **9**, 3005–3014.
54 C. A. Class, M. Liu, A. G. Vandeputte and W. H. Green, *Phys. Chem. Chem. Phys.*, 2016, **18**, 21651–21658.
55 G. A. Seisenbaeva and V. G. Kessler, *Nanoscale*, 2014, **6**, 6229–6244.
56 S. Mishra and S. Daniele, *Chem. Rev.*, 2015, **115**, 8379–8448.
57 S. Mishra, S. Daniele and L. G. Hubert-Pfalzgraf, *Chem. Soc. Rev.*, 2007, **36**, 1770–1787.
58 S. L. Benjamin, C. H. (Kees) de Groot, C. Gurnani, A. L. Hector, R. Huang, K. Ignatyev, W. Levason, S. J. Pearce, F. Thomas and G. Reid, *Chem. Mater.*, 2013, **25**, 4719–4724.
59 Y. Chang, A. L. Hector, W. Levason, G. Reid and J. Whittam, *Dalton Trans.*, 2018, **47**, 2406–2414.
60 C. Gurnani, S. L. Hawken, A. L. Hector, R. Huang, M. Jura, W. Levason, J. Perkins, G. Reid and G. B. G. Stenningd, *Dalton Trans.*, 2018, **47**, 2628–2637.
61 S. Mishra, E. Jeanneau and S. Daniele, *Polyhedron*, 2010, **29**, 500–506.
62 K. T. Higa and K. A. Fallis, *J. Cluster Sci.*, 2002, **13**, 533–541.
63 S. Schulz, S. Heimann, J. Friedrich, M. Engenhorst, G. Schierning and W. Assen-macher, *Chem. Mater.*, 2012, **24**, 2228–2234.
64 S. Heimann, W. Assenmacher, O. Prymak and S. Schulz, *Eur. J. Inorg. Chem.*, 2015, 2407–2415.
65 G. Bendt, A. Weber, S. Heimann, W. Assenmacher, O. Prymak and S. Schulz, *Dalton Trans.*, 2015, **44**, 14272–14280.
66 S. Heimann, S. Schulz, J. Schaumann, A. Mudring, J. Stotzel and G. Schierning, *J. Mater. Chem. C*, 2015, **3**, 10375–10380.
67 J. Schaumann, M. Loor, D. Unal, A. Mudring, S. Heimann, U. Hagemann, S. Schulz, F. Maculewicz and G. Schierning, *Dalton Trans.*, 2017, **46**, 656–668.
68 M. Loor, G. Bendt, U. Hagemann, C. Wolper, W. Assenmacher and S. Schulz, *Dalton Trans.*, 2016, **45**, 15326–15335.
69 G. Gupta and J. Kim, *J. Chem. Soc., Dalton Trans.*, 2013, **42**, 8209–8211.
70 G. Bendt, S. Gassa, F. Rieger, C. Jooss and S. Schulz, *J. Cryst. Growth*, 2018, **490**, 77–83.
71 K. T. Higa and K. A. Fallis, *J. Cluster Sci.*, 2002, **13**, 533–541.
72 M. Gomez, C. Hernandez-Prieto, A. Martín, M. Mena and C. Santamaría, *Inorg. Chem.*, 2016, **55**, 3815–3821.
73 J. P. Eußner, R. O. Kusche and S. Dehnen, *Chem. – Eur. J.*, 2015, **21**, 12376–12388.
74 G. Bendt, A. Weber, S. Heimann, W. Assenmacher, O. Prymak and S. Schulz, *Dalton Trans.*, 2015, **44**, 14272–14280.
75 E. Dornsiepen and S. Dehnen, *Dalton Trans.*, 2019, **48**, 3671–3675.
76 D. Fuhrmann and H. Krautscheid, *Z. Anorg. Allg. Chem.*, 2022, DOI: **10.1002/zaac.202200099**.
77 M. A. Fard, F. Weigend and J. F. Corrigan, *Chem. Commun.*, 2015, **51**, 8361–8364.
78 M. W. DeGroot and J. F. Corrigan, *Organometallics*, 2005, **24**, 3378–3385.
79 M. A. Fard, T. I. Levchenko, C. Cadogan, W. J. Humenny and J. F. Corrigan, *Chem. – Eur. J.*, 2016, **22**, 4543–4550.
80 H. Lu and R. L. Brutchey, *Chem. Mater.*, 2017, **29**, 1396–1403.
81 M. A. Hine and G. D. Scholes, *Adv. Mater.*, 2003, **15**, 1844–1849.
82 J. Tang, L. Brzozowski, D. A. R. Barkhouse, X. Wang, R. Debnath, R. Wolowiec, E. Palmiano, L. Levina, A. G. Pattantyus-Abraham and D. Jamakosmanovic, *ACS Nano*, 2010, **4**, 869–878.
83 N. Zhao, T. P. Osedach, L.-Y. Chang, S. M. Geyer, D. Wanger, M. T. Binda, A. C. Arango, M. G. Bawendi and V. Bulovic, *ACS Nano*, 2010, **4**, 3743–3752.
84 N. J. Thompson, M. W. B. Wilson, D. N. Congreve, P. R. Brown, J. M. Scherer, T. S. Bischof, M. Wu, N. Geva, M. Welborn, T. V. Voorhis, V. Bulovic, M. G. Bawendi and M. A. Baldo, *Nat. Mater.*, 2014, **13**, 1039–1043.
85 A. Stavrinadis, D. So and G. Konstantatos, *J. Phys. Chem. C*, 2016, **120**, 20315–20322.
86 J. Zhang, J. Gao, E. M. Miller, J. M. Luther and M. C. Beard, *ACS Nano*, 2014, **8**, 614–622.
87 Y. Zhang, G. Wu, C. Ding, F. Liu, Y. Yao, Y. Zhou, C. Wu, N. Nakazawa, Q. Huang, T. Toyoda, R. Wang, S. Hayase, Z. Zou and Q. Shen, *J. Phys. Chem. Lett.*, 2018, **9**, 3598–3603.
88 J. Akhtar, M. A. Malik, P. O'Brien, K. G. U. Wijayantha, R. Dharmadasa, S. J. O. Hardman, D. M. Graham, B. F. Spencer, S. K. Stubbs, W. R. Flavell, D. J. Binks, F. Sirotti, M. El Kazzi and M. Silly, *J. Mater. Chem.*, 2010, **20**, 2336–2344.
89 H. Zhang, B. H. Savitzky, J. Yang, J. T. Newman, K. A. Perez, B.-R. Hyun, L. F. Kourkoutis, T. Hanrath and F. W. Wise, *Chem. Mater.*, 2016, **28**, 127–134.
90 A. Shrestha, M. Batmunkh, A. Tricoli, S. Z. Qiao and S. Dai, *Angew. Chem., Int. Ed.*, 2019, **58**, 5202–5224.
91 A. Antanovich, A. Prudnikau and M. Artemyev, *J. Phys. Chem. C*, 2014, **118**, 21104–21109.
92 D. K. Smith, J. M. Luther, O. E. Semonin, A. J. Nozik and M. C. Beard, *ACS Nano*, 2011, **5**, 183–190.
93 J. Akhtar, M. Afzaal, M. Banski, A. Podhorodecki, M. Syperek, J. Misiewicz, U. Bangert, S. J. O. Hardman, D. M. Graham and W. R. Flavell, *J. Am. Chem. Soc.*, 2011, **133**, 5602–5609.
94 G. Shen, M. Chen and P. Guyot-Sionnest, *J. Phys. Chem. Lett.*, 2017, **8**, 2224–2228.
95 P. Glaser, O. Stewart, Jr., R. Atif, D. R. C. Asuigui, J. Swanson, A. J. Biacchi, A. R. H. Walker, G. Morrison, H.-C. zur Loye and S. L. Stoll, *Angew. Chem., Int. Ed.*, 2021, **60**, 23134–23141.
96 V. A. Ermakov, J. M. C. S. Filho, L. G. Bonato, N. V. V. Mogili, F. E. Montoro, F. Iikawa, A. F. Nogueira, C. L. Cesar, E. Jimenez-Villar and F. C. Marques, *ACS Omega*, 2018, **3**, 2027–2032.
97 (*a*) S. Schulz, S. Heimann, K. Kaiser, O. Prymak, W. Assenmacher, J. T. Bruggemann, B. Mallick and A. V. Mudring, *Inorg. Chem.*, 2013, **52**, 14326–14333; (*b*) J. M. Hwang, J. H. Lee, H.-S. Kim, C. W. Park, D. Yoo, B. K. Park, C. G. Kim and T.-M. Chung, *Polyhedron*, 2020, **176**, 14289–114294.
98 M. Rusek, G. Bendt, C. Wölper and S. Schulz, *Eur. J. Inorg. Chem.*, 2016, 3673–3679.
99 B. Zhou, M. Li, Y. Wu, C. Yang, W. H. Zhang and C. Li, *Chem. – Eur. J.*, 2015, **21**, 11143–11151.

100 P. M. Allen and M. G. Bawendi, *J. Am. Chem. Soc.*, 2008, **130**, 9240–9241.
101 S. Jung, J.-H. Cha and D.-Y. Jung, *Thin Solid Films*, 2016, **603**, 243–248.
102 M. Loor, G. Bendt, J. Schaumann, U. Hagemann, M. Heidelmann, C. Wolper and S. Schulz, *Z. Anorg. Allg. Chem.*, 2017, **643**, 60–68.
103 S. Salloum, G. Bendt, M. Heidelmann, K. Loza, S. Bayesteh, M. S. Izadi, P. Kawulok, R. He, H. Schlorb, N. Perez, H. Reith, K. Nielsch, G. Schierning and S. Schulz, *ChemistryOpen*, 2021, **10**, 189–198.
104 J. Guschlbauer and J. Sundermeyer, *ChemistryOpen*, 2021, **10**, 92–96.
105 M. Loor, S. Salloum, P. Kawulok, S. Izadi, G. Bendt, J. Guschlbauer, J. Sundermeyer, N. Perez, K. Nielsch, G. Schierning and S. Schulz, *Inorg. Chem.*, 2020, **59**, 3428–3436.
106 E. A. Turner, H. Ro1sner, D. Fenske, Y. Huang and J. F. Corrigan, *J. Phys. Chem. B*, 2006, **110**, 16261–16269.
107 E. A. Turner, H. Rosner, Y. Huang and J. F. Corrigan, *J. Phys. Chem. C*, 2007, **111**, 7319–7329.
108 A. Wolf, T. Hrtling, D. Hinrichs and D. Dorfs, *ChemPhysChem*, 2016, **17**, 717–723.
109 J. M. Hodges, K. Kletetschka, J. L. Fenton, C. G. Read and R. E. Schaak, *Angew. Chem., Int. Ed.*, 2015, **54**, 8669–8672.
110 E. E. Foos, R. M. Stroud and A. D. Berry, *Nano Lett.*, 2001, **1**, 693–695.
111 J. L. Fenton, A. M. Fagan and R. E. Schaak, *Eur. J. Inorg. Chem.*, 2019, 3490–3493.
112 J. Park, H. Zheng, Y.-W. Jun and A. P. Alivisatos, *J. Am. Chem. Soc.*, 2009, **131**, 13943–13945.
113 C. C. Lin, S. J. Tana and J. Vela, *J. Mater. Chem. A*, 2017, **5**, 20351–20358.
114 S. Schlecht, M. Budde and L. Kienle, *Inorg. Chem.*, 2002, **41**, 6001–6005.
115 P. J. McKarns, T. S. Lewkebandara, G. P. A. Yap, L. M. Liable-Sands, A. L. Rheingold and C. H. Winter, *Inorg. Chem.*, 1998, **37**, 418–424.
116 A. K. FAzlur-Rahman and J. G. Verkade, *Inorg. Chem.*, 1992, **31**, 2064–2069.
117 E. A. Turner, H. Rosner, Y. Huang and J. F. Corrigan, *J. Cluster Sci.*, 2007, **18**, 764–771.
118 E. A. Turner, H. Rosner, Y. Huang and J. F. Corrigan, *Can. J. Chem.*, 2007, **85**, 747–755.
119 D. H. Webber and R. L. Brutchey, *Chem. Commun.*, 2009, 5701–5703.
120 D. H. Webber and R. L. Brutchey, *Inorg. Chem.*, 2011, **50**, 723–725.
121 D.-J. Xue, J. Tan, J.-S. Hu, W. Hu, Y.-G. Guo and L.-J. Wan, *Adv. Mater.*, 2012, **24**, 4528–4533.
122 M. A. Franzman, C. W. Schlenker, M. E. Thompson and R. L. Brutchey, *J. Am. Chem. Soc.*, 2010, **132**, 4060–4061.
123 J. J. Buckley, F. A. Rabuffetti, H. L. Hinton and R. L. Brutchey, *Chem. Mater.*, 2012, **24**, 3514–3516.
124 M. A. Franzman and R. L. Brutchey, *Chem. Mater.*, 2009, **21**, 1790–1792.
125 M. E. Norako, M. A. Franzman and R. L. Brutchey, *Chem. Mater.*, 2009, **21**, 4299–4304.
126 D. Sun, Y. Xiong, Y. Sun, I. Dabo and R. E. Schaak, *Chem. Mater.*, 2017, **29**, 1095–1098.
127 Y.-K. Hong, Y. Park, H. Kang, H. Son and D.-H. Ha, *Dalton Trans.*, 2021, **50**, 2192–2199.
128 W. Li, A. Shavel, R. Guzman, J. Rubio-Garcia, C. Flox, J. Fan, D. Cadavid, M. Ibanez, J. Arbiol, J. R. Morantea and A. Cabot, *Chem. Commun.*, 2011, **47**, 10332–10334.
129 B. A. Tappan, W. Chu, M. Mecklenburg, O. V. Prezhdo and R. L. Brutchey, *ACS Nano*, 2021, **15**, 13463–13474.
130 B. A. Tappan, K. D. Crans and R. L. Brutchey, *Inorg. Chem.*, 2021, **60**, 17178–17185.
131 B. A. Tappan, K. D. Crans and R. L. Brutchey, *Chem. Mater.*, 2020, **32**, 2935–2945.
132 W. Wang, W. Feng, Q. Li, Y. Zhao, D. Zhao, Z. Xia, W. Wang, S. Zhang, X. Zheng and Z. Jing, *Cryst. Growth Des.*, 2019, **19**, 1226–1232.
133 P. D. Antunez, D. H. Webber and R. L. Brutchey, *Chem. Mater.*, 2013, **25**, 2385–2387.
134 J. Q. Geisenhoff, A. K. Tamura and A. M. Schimpf, *Chem. Commun.*, 2019, **55**, 8856–8859.
135 W. Jung, S. Lee, D. Yoo, S. Jeong, P. Miro, A. Kuc, T. Heine and J. Cheon, *J. Am. Chem. Soc.*, 2015, **137**, 7266–7269.
136 Y. Sun, K. Fujisawa, Z. Lin, Y. Lei, J. S. Mondschein, M. Terrones and R. E. Schaak, *J. Am. Chem. Soc.*, 2017, **139**, 11096–11105.